iScience

CellPress
OPEN ACCESS

Article

Immune-restoring CAR-T cells display antitumor activity and reverse immunosuppressive TME in a humanized ccRCC mouse model

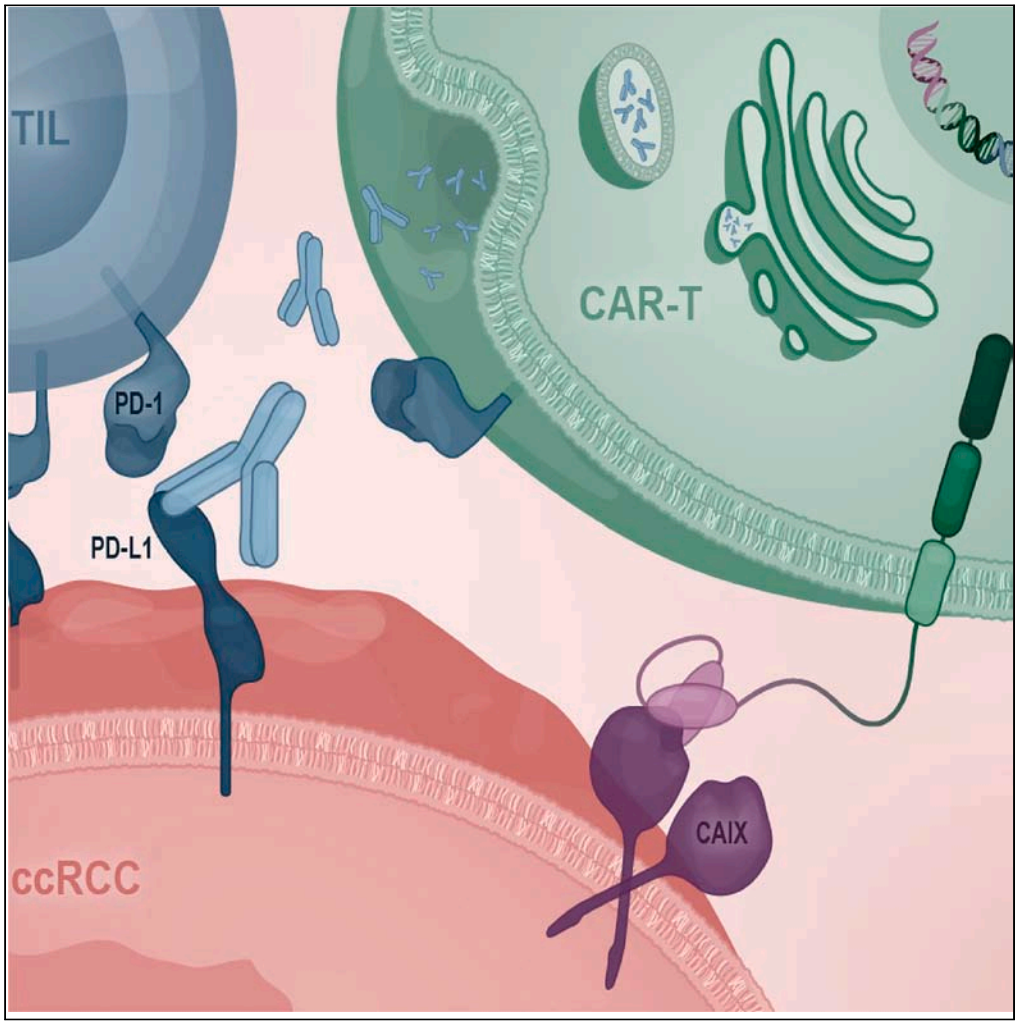

Yufei Wang, Jae-Won Cho, Gabriella Kastrunes, ..., Gordon J. Freeman, Martin Hemberg, Wayne A. Marasco

wayne_marasco@dfci.harvard.edu

Highlights

Developed immune-restoring anti-CAIX CAR-T cells secreting anti-PD-L1 mAb

A humanized ccRCC orthotopic mouse model recapitulates ccRCC patient TME

G36-PDL1 IR CAR-T shows superior antitumor efficacy in a humanized mouse model

G36-PDL1 IR CAR-T promotes tumor killing by reversing immunosuppressive TME

Wang et al., iScience 27, 108879
February 16, 2024 © 2024
https://doi.org/10.1016/j.isci.2024.108879

iScience

CellPress
OPEN ACCESS

Article

Immune-restoring CAR-T cells display antitumor activity and reverse immunosuppressive TME in a humanized ccRCC mouse model

Yufei Wang,[1,2,11] Jae-Won Cho,[2,3,11] Gabriella Kastrunes,[1] Alicia Buck,[1] Cecile Razimbaud,[1] Aedin C. Culhane,[4] Jiusong Sun,[1] David A. Braun,[2,5,6] Toni K. Choueiri,[2,5] Catherine J. Wu,[2,5] Kristen Jones,[7] Quang-De Nguyen,[7] Zhu Zhu,[2,8] Kevin Wei,[2,8] Quan Zhu,[1,2] Sabina Signoretti,[2,9,10] Gordon J. Freeman,[2,5] Martin Hemberg,[2,3,12] and Wayne A. Marasco[1,2,12,13,*]

SUMMARY

One of the major barriers that have restricted successful use of chimeric antigen receptor (CAR) T cells in the treatment of solid tumors is an unfavorable tumor microenvironment (TME). We engineered CAR-T cells targeting carbonic anhydrase IX (CAIX) to secrete anti-PD-L1 monoclonal antibody (mAb), termed immune-restoring (IR) CAR G36-PDL1. We tested CAR-T cells in a humanized clear cell renal cell carcinoma (ccRCC) orthotopic mouse model with reconstituted human leukocyte antigen (HLA) partially matched human leukocytes derived from fetal CD34$^+$ hematopoietic stem cells (HSCs) and bearing human ccRCC skrc-59 cells under the kidney capsule. G36-PDL1 CAR-T cells, haploidentical to the tumor cells, had a potent antitumor effect compared to those without immune-restoring effect. Analysis of the TME revealed that G36-PDL1 CAR-T cells restored active antitumor immunity by promoting tumor-killing cytotoxicity, reducing immunosuppressive cell components such as M2 macrophages and exhausted CD8$^+$ T cells, and enhancing T follicular helper (Tfh)-B cell crosstalk.

INTRODUCTION

Immunotherapy is revolutionizing the practice of medical oncology, and chimeric antigen receptor (CAR) T cell therapy has proven to be effective for hematologic malignancies; however, several barriers have restricted CAR-T in the treatment of solid tumors.[1–12] While inefficient CAR-T cell homing and metabolic changes have been shown to contribute to treatment inefficiencies in solid tumors, the immunosuppressive tumor microenvironment (TME) is known to be a major barrier to the translation of CAR-T cell therapy into solid tumors due to commandeering of the immune system causing T cell exhaustion and anti-inflammatory polarizations.[11,13]

Clear cell renal cell carcinoma (ccRCC) is the major histological subtype of RCC and has a paradoxical correlation that CD8$^+$ T cell infiltration is associated with a worse prognosis.[14] Thus, understanding the ccRCC TME is a necessary step to thwart disease progression and response to immunotherapy.[15] Chevrier et al. observed an association between CD38$^+$ CD204$^+$ CD206$^-$ tumor-associated macrophages (TAMs) and immunosuppression within the ccRCC TME.[16] Moreover, advanced stage patients with loss of 9p21.3 were found to have increased immune infiltration, and were less responsive to PD-1 blockade, with worse progression-free survival (PFS) and overall survival (OS).[17] Thus, we hypothesize that understanding the PD-1 resistance found in ccRCC will provide immunotherapy targets to restore active antitumor immunity.

Single-cell RNA sequencing (scRNA-seq) has emerged as a powerful tool for gaining important insights regarding the TME in ccRCC[18,19] and other cancers.[20–22] Recently, advancing ccRCC disease state was shown to demonstrate not only increased exhausted CD8$^+$ T cells and

[1]Department of Cancer Immunology and Virology, Dana-Farber Cancer Institute, Boston, MA 02215, USA
[2]Harvard Medical School, Boston, MA 02215, USA
[3]Gene Lay Institute of Immunology and Inflammation, Brigham and Women's Hospital, Boston, MA 02115, USA
[4]School of Medicine, University of Limerick, V94 T9PX Limerick, Ireland
[5]Department of Medical Oncology, Dana-Farber Cancer Institute, Boston, MA 02215, USA
[6]Center of Molecular and Cellular Oncology, Yale Cancer Center, Yale School of Medicine, New Haven, CT 06525, USA
[7]Lurie Family Imaging Center, Center for Biomedical Imaging in Oncology, Dana-Farber Cancer Institute, Boston, MA 02215, USA
[8]Division of Rheumatology, Inflammation and Immunity, Brigham and Women's Hospital, Boston, MA 02115, USA
[9]Department of Oncologic Pathology, Dana-Farber Cancer Institute, Boston, MA 02215, USA
[10]Department of Pathology, Brigham and Women's Hospital, Boston, MA 02115, USA
[11]These authors contributed equally
[12]Co-senior authors
[13]Lead contact
*Correspondence: wayne_marasco@dfci.harvard.edu
https://doi.org/10.1016/j.isci.2024.108879

M2-like macrophages, but also that crosstalk between exhausted CD8$^+$ T and M2 cells forms a dysfunctional immune circuit which promotes further T cell exhaustion and M2-like polarization, leading to a worse prognosis.[18]

Prior immunotherapy research in ccRCC has been hampered by the limited availability of murine tumor cell lines. Moreover, while genetically engineered models that harbor mutations that lead to the development of kidney cancer closely matching those observed in humans have been generated, they are only useable in immunocompetent syngeneic mice.[23,24] We assert that due to inter-species differences in the immune system, a murine model with a humanized immune system is required to accurately reconstitute a TME which more closely matches that of cancer patients. Such a model would certainly allow for a better understanding of the interplay between human immune cells in the ccRCC TME, and provides a powerful tool for immunotherapy development and assessment of agents that might be directly translated to humans.[25–27] Indeed, CD34$^+$ progenitor hematopoietic stem cells (HSCs)-derived humanized mouse models provide the ability to study antitumor effects, such as response to immune checkpoint inhibitors (ICI)[28] in a physiologically relevant immune environment.[29]

Here, we established a humanized ccRCC orthotopic NSG-SGM3 mouse model (termed hccRCC-NSG-SGM3) using human leukocyte antigen (HLA) partially matched CD34$^+$ HSCs isolated from fetal liver, which recapitulates the ccRCC patient TME, and presents the same pattern of increased exhausted T cells (Tex) and M2-like macrophages as observed in advanced human ccRCC.[18] Using this model, we evaluated anti-carbonic anhydrase IX (CAIX) immune-restoring (IR) CAR-T cells which were constructed based on our previous work using 4-1BB costimulatory domain and ICI payload.[30,31] The IR CAR-T cells secreting anti-PD-L1 monoclonal antibody (mAb) exhibited superior tumor-killing capacity and the ability to restore active antitumor immunity by overcoming PD-1 resistance of ccRCC. Profiling tumor-infiltrating leukocytes (TILs) via scRNA-seq showed that IR CAR-T cells attenuate the immunosuppression in the TME and maintain a favorable antitumor phenotype in this humanized ccRCC mouse model.

RESULTS

Generation of IR CAR-T cells

CAIX is highly expressed in ccRCC as a downstream gene of the HIF pathway[32,33] and has been utilized as a therapeutic target for ccRCC therapy.[34–36] Previously, we demonstrated that anti-CAIX G36-CD28 CAR-T cells secreting human ICI mAbs locally reduced CAR-T cell exhaustion in the tumor using a ccRCC orthotopic NSG mouse model without a human TME.[30] In addition, we demonstrated that CAIX-specific CAR-T with a 4-1BB signaling domain (G36-4-1BB (BBζ)) outperformed both CD28 domain (G36-CD28 (28ζ)) and combined domain (G36-CD28-4-1BB (28BBζ)) and that BBζ with a CD8:CD4 ratio of 1:2 exhibited superior efficacy and persistence *in vivo*.[31] Building on these results, we engineered anti-CAIX G36 BBζ CAR-T cells secreting anti-PD-L1 mAb (G36-PDL1) (Table S1). The PD-L1 mAb was expressed as a scFv with a human IgG4 Fc with mutations in the hinge to stabilize the structure (termed scFv-Fc).[37] We assessed the efficacy of these IR CAR-T cells *in vitro* using the ccRCC skrc-59 cell line and *in vivo* in the hccRCC-NSG-SGM3 model. To control for CAR specificity and antibody payload, we used anti-B cell maturation antigen (BCMA) A716 CAR-T cells secreting anti-PD-L1 scFv-Fc (A716-PDL1) and anti-CAIX G36 CAR-T cells secreting anti-SARS scFv-Fc (G36-SARS), respectively (Figure 1A; Table S1).

Characterization of IR CAR-T cells *in vitro*

We assessed tumor killing by IR CAR-T cells after 48 h co-incubation with CAIX+ PD-L1+ skrc-59 cells by using an image-based cytotoxicity assay.[38] At an effector:target (E:T) ratio of 10:1 and CD8:CD4 ratio of 1:2, both G36-PDL1 and G36-SARS exhibited ~95% killing capacity *in vitro*, while A716-PDL1 only exhibited modest cytotoxicity at levels similar to the untransduced T cells (UNT) (Figure 1B). At different E:T ratios, G36-PDL1 showed significantly higher tumor killing compared to A716-PDL1 and UNT but not G36-SARS. After 48 h co-incubation, G36-PDL1 exhibited a lower percentage of terminally exhausted T cells (PD-1hi TIM-3+) (Figure 1C) and a higher percentage of effector memory T cells (Tem) (Figure 1D) compared to G36-SARS CAR-T cells. We conclude that the anti-PD-L1 mAb secreted by G36-PDL1 CAR-T cells contributed to the lower exhaustion, higher Tem percentage, and increased CD8:CD4 ratio (Figure S1A) in G36-PDL1 CAR-T cells compared to G36-SARS CAR-T cells. Quantification of antibody production showed that all IR CAR-T cells secreted mAbs at a rate of ~0.1 pg/cell/day (Figure 1E).

G36-PDL1 CAR-T cells exhibited superior efficacy *in vivo* in hccRCC-NSG-SGM3 model

To assess the ability of IR CAR-T cells to control tumor growth *in vivo*, we established the hccRCC-NSG-SGM3 mouse model (Figure 2A). Human CD34$^+$ HSCs that were partially HLA (HLA-A, HLA-B, HLA-C, DRB1) matched to human ccRCC skrc-59 were isolated from fetal liver and injected intrahepatically into irradiated neonates (1–4 days) (Figures 2B and 2C). Once humanization was mature (greater than 20% circulating human lymphocytes), luciferized CAIX+ PD-L1+ human ccRCC skrc-59 tumor cells were implanted under the kidney capsule to establish ccRCC orthotopic humanized NSG-SGM3 mouse model[31] which was further validated. Tumor-bearing humanization matured mice were divided into 5 groups with similar immune cell reconstruction efficiency as indicated by human CD45 positivity (Figure 2B), then a single dose of one million CAR-T cells (CD8:CD4 = 1:2) was injected through the tail vein. CAR-T cells were 6/6 HLA haploidentical (HLA-A, HLA-B, HLA-C, DRB1, DQB1, DPB1) to human ccRCC skrc-59 (Figure 2C). Bioluminescence imaging (BLI) was performed to monitor tumor growth and peripheral blood was analyzed to characterize humanization and peripheral circulating immune cells *in vivo*. Four weeks later, tumors were collected and digested into single-cell suspensions.

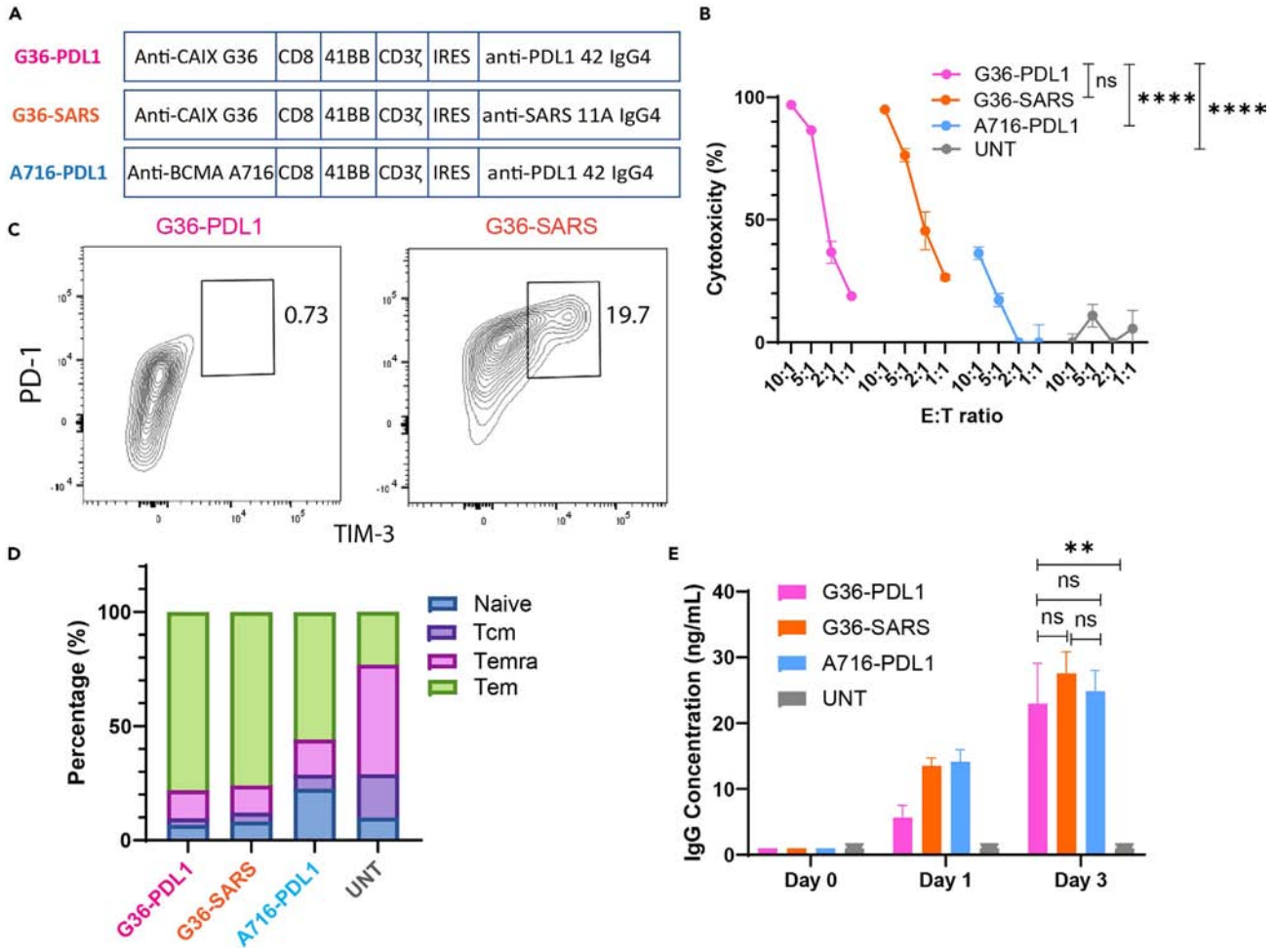

Figure 1. Anti-CAIX G36-PDL1 CAR-T cells secreting anti-PD-L1 IgG4 payload lowered exhaustion *in vitro*

(A) The schematic shows G36-PDL1 (pink), G36-SARS (orange), and A716-PDL1 (blue) CAR constructs.

(B) Cytotoxicity of G36-PDL1 (pink), G36-SARS (orange), and A716-PDL1 (blue) CAR-T cells, and untransduced T cells (UNT, gray) with CD8:CD4 ratio of 1:2 under E:T ratio of 10:1, 5:1, 2:1, and 1:1 on CAIX^{+} ccRCC skrc-59 tumor cells.

(C) Percentage of terminally exhausted T cells (PD1^{hi}, TIM-3^{+}) of G36-PDL1 (pink), and G36-SARS (orange) CAR-T cells.

(D) Percentage of naive T cell (Naive, blue), central memory T cell (Tcm, purple), effector memory T cell re-expressing CD45RA (Temra, magenta), and effector memory T cell (Tem, green) of G36-PDL1 (pink), G36-SARS (orange), A716-PDL1 (blue), and CAR-T cells and UNT cells (gray) after 48 h co-incubation with skrc-59 tumor cells.

(E) Payload secretion quantification of G36-PDL1 (pink), G36-SARS (orange), A716-PDL1 (blue), and CAR-T cells and UNT cells (gray). All data with error bars are presented as mean ± SD. p values are defined by unpaired two-tailed t-tests or two-way ANOVA (*$p < 0.05$; **$p < 0.01$; ***$p < 0.001$; and ****$p < 0.0001$).

Mice treated with G36-PDL1 IR CAR-T cells exhibited superior tumor regression two weeks after a single-dose administration compared to G36-SARS, A716-PDL1, UNT, and PBS as shown in BLI (Figures 2D, 2E, and S2). The kinetics of immune cell expansion were documented and compared to the day of CAR-T cell infusion (day 0) (Figures S1B–S1E).

The hccRCC-NSG-SGM3 mouse model recapitulated human immunity and treatment broadly altered TME landscape

Tumor-infiltrating human CD45^{+} cells were sorted and profiled for transcriptome and proteome via scRNA-seq, single-cell T cell receptor sequencing (scTCR-seq), and flow cytometry to study the TME, including population abundances and gene expression among the three CAR-T cell-treated groups (Group 1: G36-PDL1 CAR-T, Group 2: G36-SARS CAR-T, Group 3: A716-PDL1 CAR-T), and two TME baseline groups (Group 4: UNT, and Group 5: PBS) (Figure 3A). After quality control and batch correction (see STAR methods and Figure S3), 14,663 TILs composed of T cells (expressing *CD3D*, *CD3E*, and *CD3G*), B cells (expressing *CD19*, *CD79A*, *MS4A1*/CD20), and myeloid cells (expressing *SPP1*, *TPSAB1*, *TPSB2*, *CD14*, and *CD68*) were recovered (Figures 3B and 3C; Tables S2 and S3). Comparison to patient data from prospective clinical trials of advanced ccRCC patients[18] revealed that the TILs from our hccRCC-NSG-SGM3 mouse model reconstituted most CD45^{+} cell types observed in patient ccRCC TME, suggesting similar landscape as human TILs (Figures 3D, 3E, and S4).

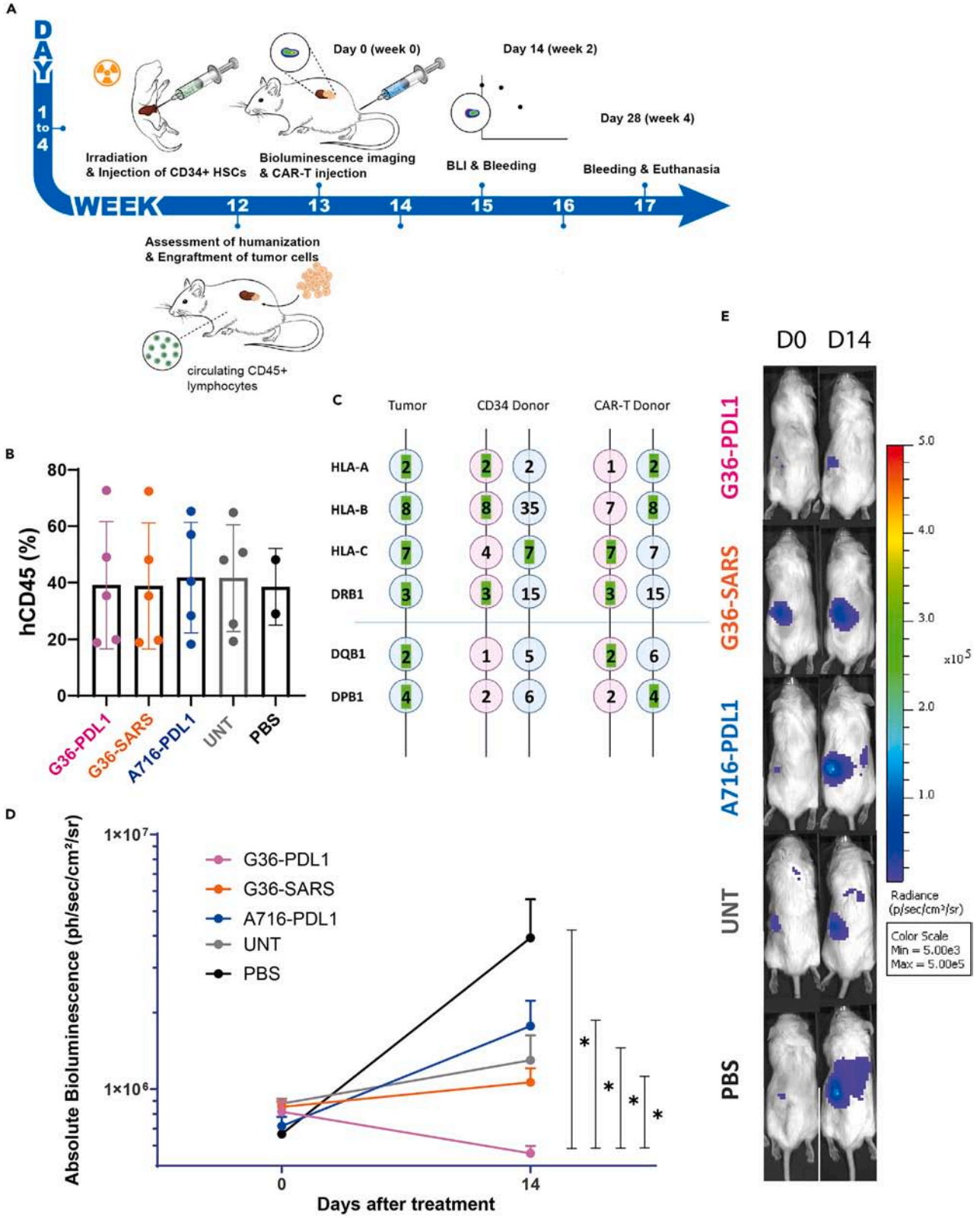
A
DAY 1 to 4
Irradiation
& Injection of CD34+ HSCs
Day 0 (week 0)
Bioluminescence imaging
& CAR-T injection
Day 14 (week 2)
BLI & Bleeding
Day 28 (week 4)
Bleeding & Euthanasia
WEEK 12 13 14 15 16 17
Assessment of humanization
& Engraftment of tumor cells
circulating CD45+
lymphocytes
B
hCD45 (%)
80
60
40
20
0
G36-PDL1
G36-SARS
A716-PDL1
UNT
PBS
C
Tumor
CD34 Donor
CAR-T Donor
HLA-A 2 2 2 1 2
HLA-B 8 8 35 7 8
HLA-C 7 4 7 7 7
DRB1 3 3 15 3 15
DQB1 2 1 5 2 6
DPB1 4 2 6 2 4
D
Absolute Bioluminescence (ph/sec/cm²/sr)
1×10⁷
1×10⁶
G36-PDL1
G36-SARS
A716-PDL1
UNT
PBS
0
14
Days after treatment
*
*
*
*
E
D0 D14
G36-PDL1
G36-SARS
A716-PDL1
UNT
PBS
5.0
4.0
3.0
x10⁵
2.0
1.0
Radiance
(p/sec/cm²/sr)
Color Scale
Min = 5.00e3
Max = 5.00e5

Figure 2. Anti-CAIX G36-PDL1 CAR-T cells exhibited superior tumor regression compared to G36-SARS and A716-PDL1 CAR-T cells in a humanized ccRCC orthotopic NSG-SGM3 mouse model

(A) The schematic shows the establishment of the hccRCC-NSG-SGM3 mouse model and how it is used to assess different treatments. $CD34^+$ HSCs were injected intrahepatically into 1–4 days old neonates. 12 weeks later, the humanization was assessed. Once the humanization was mature, ccRCC skrc-59 tumor cells were inoculated under the kidney capsule. One week after tumor implantation, one million CAR-T cells, UNT cells, or 100 μl of PBS were injected intravenously. Tumor growth was monitored by BLI at day 0 and 14 and human immunity and circulating CAR-T were phenotyped by weekly bleeding.

(B) Humanization efficiency (the percentage of human $CD45^+$ immune cells out of total live leukocytes in the peripheral blood) in G36-PDL1 (pink), G36-SARS (orange), A716-PDL1 (blue) CAR-T cells, UNT cells (gray), PBS (black) is shown in the bar plot. Peripheral blood was analyzed via flow cytometry. Each dot represents one mouse.

(C) HLA phenotype of ccRCC skrc-59 tumor cells, $CD34^+$ HSC donor and CAR-T donor. HLA-A, HLA-B, HLA-C, DRB1, DQB1, and DPB1 are shown here. Green highlights indicate HLA match.

(D) Tumor growth curve of the mice treated with one million CD8:CD4 = 1:2 G36-PDL1 (pink), G36-SARS (orange), A716-PDL1 (blue) CAR-T cells, UNT cells (gray) or PBS (black).

(E) Representative BLI images of mice treated with one million CD8:CD4 = 1:2 G36-PDL1 (pink), G36-SARS (orange), A716-PDL1 (blue) CAR-T cells, UNT cells (gray) or PBS (black). All data with error bars are presented as mean ± SD. p values are defined by unpaired two-tailed t-tests (*$p < 0.05$; **$p < 0.01$; ***$p < 0.001$; and ****$p < 0.0001$).

While T cell infiltration was similar in all 5 groups, G36-PDL1 had significantly higher B cell infiltration (Fold change (q value) of group1 vs. group2: 2.22 (3.67E-6); vs. group3: 26.3 (1.47E-36); vs. group4: 5.22 (1.82E-4); vs. group5: 2.03 (9.91E-2)) and lower myeloid infiltration (Fold change (q value) of group1 vs. group2: 0.147 (1.74E-38); vs. group3: 1.04 (8.26E-1); vs. group4: 0.544 (9.00E-2); vs. group5: 0.0326 (1.05E-103)), especially of $CD163^+$ M2-like macrophages (Figures 3F and 3G, and specific cell number and abundance are shown in Table S4). We thus hypothesized that anti-PD-L1 mAb affects the immune response and TME in a way that inhibits M2 macrophage polarization[39,40] and enhances B cells infiltration into G36-PDL1 TME. Our data implicate B cells in G36-PDL1 contributed to the anti-tumor effect. Although B cell influence on RCC TME remains unclear,[41–43] a role for B cells in the antitumor immune response is emerging.[44–47]

G36-PDL1 CAR-T cells maintain a distinct cellular composition and function at the tumor site

Endogenous T cells, CAR-T cells, NK cells, and NKT cells were further clustered into 19 sub-clusters (Figures 4A and 4B), and each cell type was annotated based on differentially expressed genes (DEGs) (Tables S3 and S5). We identified nine $CD8^+$ T subclusters (Figure 4C) and seven $CD4^+$ subclusters (Figure 4D), a $CD4^-$ $CD8^-$ T subcluster, an NKT subcluster, and an NK subcluster (Figure S5). CAR-T cells were identified by the expression of the G36 CAR sequence and the A716 CAR sequence (Figure 4B; Table S1). Since 242 of 248 G36 CAR^+ T cells were from G36-PDL1, we considered the recovered G36 CAR-T cells stemmed from the G36-PDL1 construct.

G36 CAR-T cells were predominantly found in the Cytotoxic_CD8_T_2 (G36 $CD8^+$ CAR-T) and TFH_2 (G36 $CD4^+$ CAR-T) clusters. A716 CAR-T cells were also contained in the TFH_2 cluster but in addition, in other clusters composed of cycling T cells, Cytotoxic_CD8_T_1, Cytotoxic_CD4_T, CM_CD4_T, and TFH_2 (Figure 4B). These data indicate that A716 $CD4^+$ CAR-T cells share similar diverse status to the endogenous $CD4^+$ T cells that are derived from reconstituted human bone marrow and do not express CAR, while G36 $CD4^+$ CAR-T cells are skewed toward a phenotype which is more favorable for immune response as shown in Figure 2.

Cytotoxic_CD8_T_1 and Cytotoxic_CD8_T_2 showed the highest expression of cytotoxicity-related genes compared to other $CD8^+$ T cell subsets (Figure 4C; Table S5) along with high expression of MHC class II molecules, indicating these CAR-T cells are highly activated[31] (Figure S6B). However, Cytotoxic_CD8_T_1 showed high GZMK expression, indicating $CD8^+$ A716-PDL1 CAR-T dysregulation at the tumor site.[48,49] Moreover, by using RNA velocity[50] analysis to estimate transition probabilities between the different T cell subsets, we found that Cytotoxic_CD8_T_2, one of the most cytotoxic subsets found in G36-PDL1 CAR-T cells, was more likely to retain its state rather than to differentiate into other states (Figures 5A, S8, and S9; Table S6).

G36-PDL1 rewired endogenous TME with high cytotoxic $CD8^+$ T and low Treg infiltration

We identified two other cytotoxic endogenous T cell subsets (Cytotoxic_CD8_T_3 and Cytotoxic_CD8_T_4) with high cytotoxicity and high NK signature gene expression, as well as one Activated_CD8_T cell subset with interferon-induced factors and IFNG[51,52] (Figure 4C). Comparing the distribution of T cell subsets in each group, G36-PDL1 showed enhanced functional cytotoxic $CD8^+$ CAR-T and endogenous T cell infiltration (Cytotoxic_CD8_T_2, Cytotoxic_CD8_T_4, Activated_CD8_T) (Figure S6A), which was likely due to the anti-PD-L1 payload promoting favorable antitumor immunity.[53]

In addition to the different subclusters composition described previously, we observed a lower abundance of CD8_Treg (Fold change of group1 vs. group2: 0.32) and CD4_Treg (Fold change of group1 vs. group2: 0.24) (*FOXP3*, *IL2RA/CD25*, *TNFRSF9/4-1BB*, *CCR8*, and immune checkpoint molecules) (Table S4)[45,54] in the G36-PDL1 TME compared to G36-SARS (Figure S6A). Furthermore, comparison of the clonotypes found in $CD4^+$ Treg and the other $CD4^+$ T cell subsets using Jaccard coefficient revealed a lower similarity score in the G36-PDL1 group (Figure S7C). Since Treg can differentiate from conventional T cells,[55] and anti-PD-L1 mAb inhibits differentiation of induced Treg,[56] the lower Jaccard coefficient observed in G36-PDL1 indicates that the ICI payload changes TME conditions so they maintain active antitumor immunity but are unfavorable to support Treg differentiation.

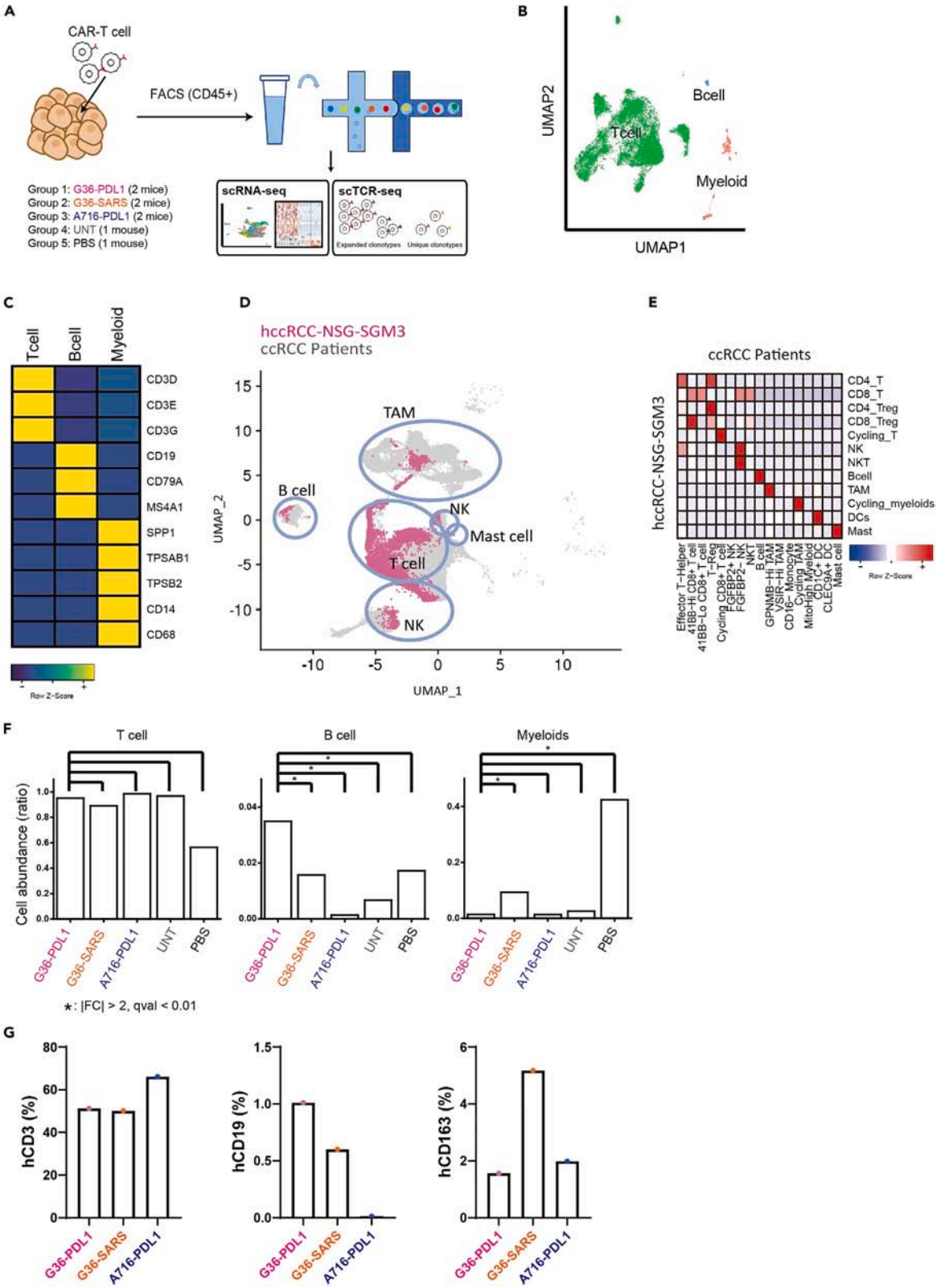
A
CAR-T cell
FACS (CD45+)
Group 1: G36-PDL1 (2 mice)
Group 2: G36-SARS (2 mice)
Group 3: A716-PDL1 (2 mice)
Group 4: UNT (1 mouse)
Group 5: PBS (1 mouse)
scRNA-seq
scTCR-seq
Expended clonotypes
Unique clonotypes
B
UMAP2
UMAP1
Bcell
Tcell
Myeloid
C
Tcell
Bcell
Myeloid
CD3D
CD3E
CD3G
CD19
CD79A
MS4A1
SPP1
TPSAB1
TPSB2
CD14
CD68
Row Z-Score
D
hccRCC-NSG-SGM3
ccRCC Patients
TAM
B cell
NK
Mast cell
T cell
NK
UMAP_2
UMAP_1
E
ccRCC Patients
hccRCC-NSG-SGM3
CD4_T
CD8_T
CD4_Treg
CD8_Treg
Cycling_T
NK
NKT
Bcell
TAM
Cycling_myeloids
DCs
Mast
Effector T−Helper
41BB−Hi CD8+ T cell
41BB−Lo CD8+ T cell
Cycling CD8+ T cell
FGFBP2+ NK
FGFBP2− NK
GPNMB−Hi TAM
VSIG4+ TAM
CD16+ Monocytes
Cycling TAM
MitoHigh Myeloid
CD1C+ DC
CLEC9A+ DC
Mast cell
Row Z-Score
F
T cell
B cell
Myeloids
Cell abundance (ratio)
G36-PDL1
G36-SARS
A716-PDL1
UNT
PBS
*: |FC| > 2, qval < 0.01
G
hCD3 (%)
hCD19 (%)
hCD163 (%)
G36-PDL1
G36-SARS
A716-PDL1

Figure 3. Overall landscape of tumor microenvironment in the hccRCC-NSG-SGM3 mice treated with different CAR-T cell therapies

(A) Schematic flow of scRNA and scTCR sequencing for tumor samples. Live human CD45$^+$ TILs from five groups were sorted and profiled.

(B) UMAP plot of main cell types (T cell: green, B cell: blue, and Myeloid cells: red).

(C) Heatmap of mean expression of marker genes for each main cell types.

(D) UMAP overlay of all TILs recovered from hccRCC-NSG-SGM3 (in pink) and TILs recovered from ccRCC patients (in gray).

(E) Heatmap of the cell type mapping ratio between hccRCC-NSG-SGM3 (row) and ccRCC patients (column).

(F) Bar plots of relative cell abundance for each main cell type between different groups. * indicates a significant difference (fold change >2, q value <0.01) between two groups.

(G) Bar plots of relative cell abundance for human CD3$^+$ T, human CD19$^+$ B, and human CD163$^+$ M2-like cells between different groups assessed via flow cytometry.

The highest clonal expansion and lowest clonal diversity were observed in the G36-SARS group

T cell receptor (TCR) clonal diversity of peripheral circulating T cells is positively associated with cancer patient prognosis and ICI response.[57–59] However, the correlation between TCR clonal diversity of tumor-infiltrating T cells and prognosis and response remains unclear. We analyzed the clonal expansion and clonal diversity of tumor-infiltrating CAR-T and endogenous T cells (Figures 5B–5D). G36-SARS showed the highest clonal expansion (Fold change of group2 vs. group1: 1.27, vs. group3: 1.04, vs. group4: 1.43, vs. group5: 2.08) and the lowest clonal diversity (T: 0.96, 0.54, 0.91, 0.99, 0.98; CD8 T: 0.94, 0.36, 0.8, 0.98, 0.96) compared to other groups (Figures 5C and 5D). This finding indicates that CAIX targeted CAR-T cells alone (without ICI payload), while showing antitumor activity *in vivo*, remain susceptible to extrinsic factors in the TME that lead to TIL exhaustion. The data are also consistent with observations in tumor-infiltrating exhausted T cells in advanced stage RCC patients that high clonal expansion was associated with advanced disease stage.[19]

Clonal expansion was also reflected by the change in CD8:CD4 ratio from the 1:2 used for CAR-T administration, which we have previously shown results in better expansion, efficacy, and persistence *in vivo*.[31] Four weeks after administration, we observed higher infiltration of CD8$^+$ T cells than CD4$^+$ T cells at the tumor site (Figure S1F) (group1: 2.61, group2: 0.89, group3: 0.72). Comparing the CD8/CD4 ratio, both CAR-T (group1: 3.08, group3: 0.86) and endogenous T cells (group1: 3.54, group2: 2.06, group3: 0.85, group4: 0.30, group5: 0.73) in G36-PDL1 group showed the highest CD8/CD4 T cell ratio, indicating specific CD8 clonal expansion upon CAR or TCR activation (Figures S7A and S7B). In CD8$^+$ T cells from hccRCC-NSG-SGM3, we also observed high expression of CD39 (*ENTPD1*), a biomarker of tumor-specific CD8$^+$ TILs,[60] showing the tumor-specific response within the TME (Figure S7D).

Tumor-infiltrating T cells in G36-PDL1 TME have high cytotoxic, low exhausted, low terminally exhausted phenotype

Profiling T cell signatures among the five groups, we found that G36-PDL1 tumor-infiltrating T cells showed greater cytotoxicity, as well as lower exhaustion, terminal exhaustion, and percentage of PD1^{hi} TIM-3$^+$ T cell population compared to G36-SARS (Figures 5E and 5F) suggesting that G36-PDL1 CAR-T cells have reshaped the TME and enabled the TILs to maintain their antitumor effect. Interestingly, tumor-infiltrating A716-PDL1 CAR-T cells showed the highest cytotoxicity score and the lowest exhaustion score (Figure 5E; Table S7) but also the highest terminal exhaustion signature[18] and the most abundant PD1^{hi} TIM-3$^+$ T cell population (Figures 5E and 5F). This suggests an irreversible exhaustion state[61,62] in A716-PDL1, reflecting their poor therapeutic efficacy.

G36-PDL1 CAR-T reshaped TME into an active antitumor environment with decreased Tex-M2 crosstalk and enhanced Tfh-B cell crosstalk

Myeloid cells were further categorized into macrophages (expressing *CD14*, *CD68*), dendritic cells (expressing *CLEC10A*/*CLC10*, *CD1C*), and mast cells (*TPSAB1*/*TRYB1*, *CPA3*, *TPSB2*) (Figure 6A and S10; Table S8). Furthermore, we could distinguish M1- and M2-like macrophages by known marker genes (Figure 6B; Table S2). M2 macrophages express anti-inflammatory molecules and restrict the antitumor effect,[63] and a high abundance of M2-like macrophages leads to an unfavorable outcome in cancer immunotherapy in ccRCC patients.[17,18] The anti-PD-L1 mAb is known to inhibit M2 polarization,[39,40] and we observed the same effect in the mouse model with low abundance of M2-like macrophages in G36-PDL1 compared to G36-SARS (Figures 6C and 3G).

To explore cell-cell interactions within the TME, we used CellChat[64] and found a substantial decrease in the number of interactions between M2_like_TAM and most T subtypes in the G36-PDL1 TME compared to the G36-SARS TME (Figures 6D and S11; Table S9). DEGs analysis showed downregulation of myeloid regulators (*MIF*,[65] *CSF1*[66]) in Exhausted_TR_CD8_T_2 in the G36-PDL1 TME compared to the G36-SARS TME. This suggests an attenuated circuit between exhausted CD8 T cells and M2 cells due to the anti-PD-L1 payload (Table S9). The interactions between TFH_1, TFH_2, and B cells were enhanced in G36-PDL1 compared to the ones in other groups (Figures 6D and S11), which is consistent with reports that the interaction between T follicular helper cell (Tfh) and B cell has a favorable effect in the TME due to the formation of tertiary lymphoid structures.[43,45–47] Taken together, these results suggest that G36-PDL1 supports a more favorable TME that leads to increased tumor cell killing, decreased communication among exhausted T cells and M2 macrophages (Tex-M2), and enhanced Tfh-B cell crosstalk.

DISCUSSION

We have established a humanized ccRCC mouse model which can recapitulate cardinal features of the ccRCC human TME and serves as a powerful tool for immunotherapy assessment. The efficacy and ability to restore active immunity of IR CAR-T cells were assessed in

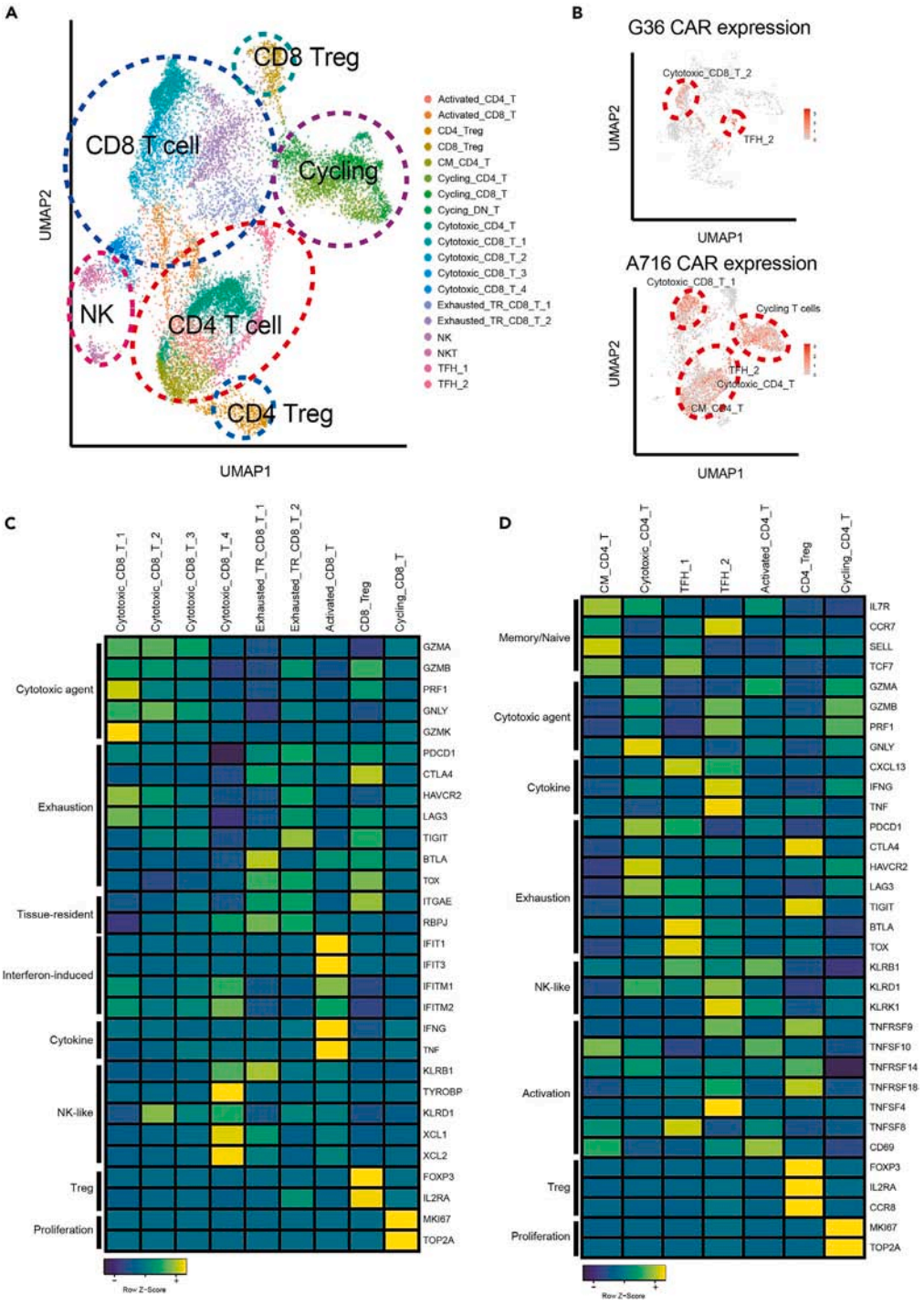

Figure 4. Landscape of tumor-infiltrating T/NK/NKT cells

(A) UMAP plot of tumor infiltrating T cell subsets for both endogenous T cells and CAR-T cells, and NK and NKT cell subsets, including 19 subclusters.

(B) The distribution of CAR-seq in T cell subsets. G36 CAR contains two major clusters Cytotoxic_CD8_2 and TFH_2 (upper panel) and A716 CAR contains Cytotoxic_CD8_T_1, Cycling T cells, TFH_2, Cytotoxic_CD4_T, CM_CD4_T (lower panel).

(C) Heatmap of mean expression of signature genes for characterizing $CD8^+$ T cell subsets.

(D) Heatmap of mean expression of signature genes for characterizing $CD4^+$ T cell subsets.

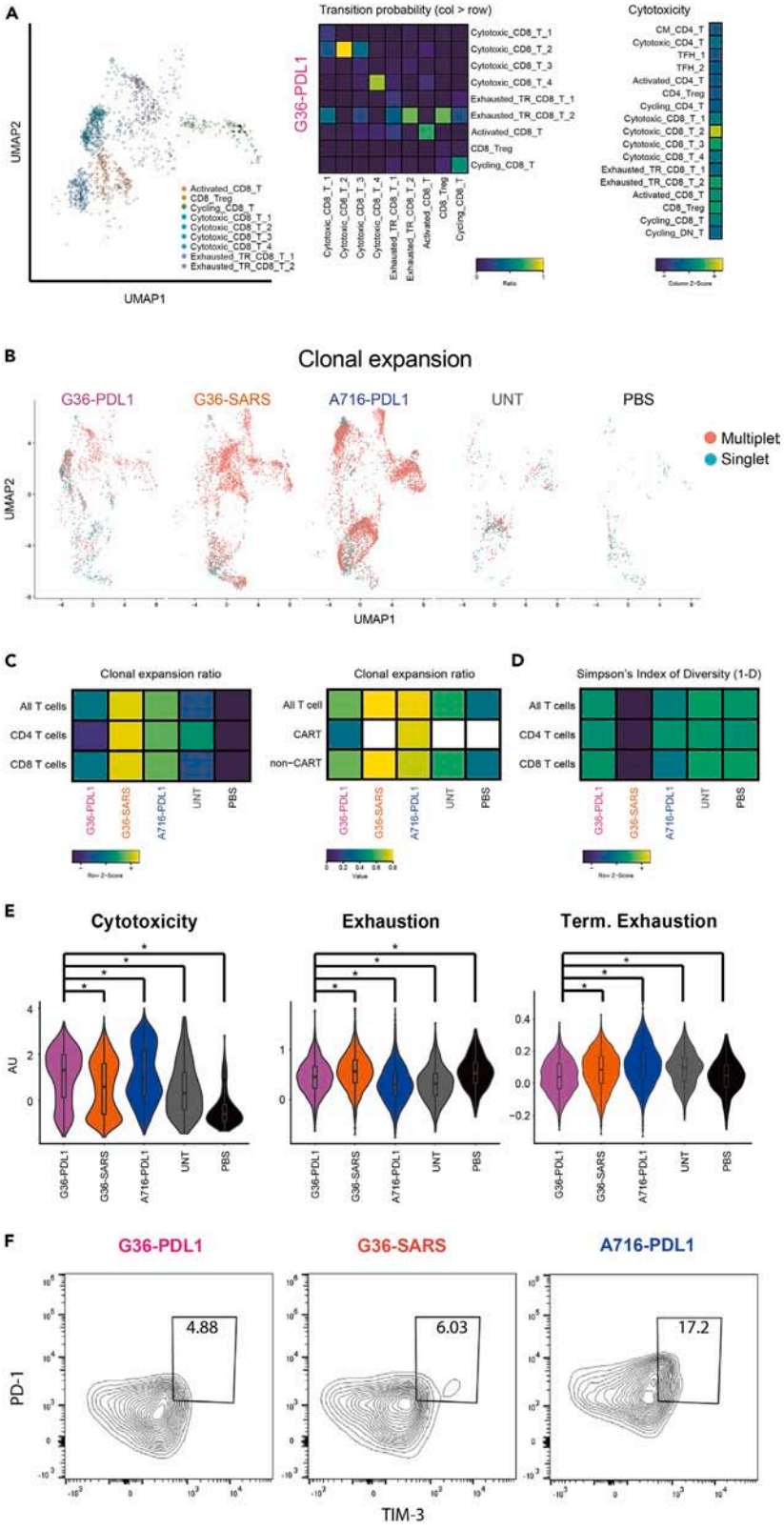
A
UMAP2
UMAP1
Activated_CD8_T
CD8_Treg
Cycling_CD8_T
Cytotoxic_CD8_T_1
Cytotoxic_CD8_T_2
Cytotoxic_CD8_T_3
Cytotoxic_CD8_T_4
Exhausted_TR_CD8_T_1
Exhausted_TR_CD8_T_2
Transition probability (col > row)
G36-PDL1
Cytotoxicity
CM_CD4_T
Cytotoxic_CD4_T
TFH_1
TFH_2
Activated_CD4_T
CD4_Treg
Cycling_CD4_T
Cycling_DN_T
B
Clonal expansion
G36-PDL1
G36-SARS
A716-PDL1
UNT
PBS
Multiplet
Singlet
C
Clonal expansion ratio
All T cells
CD4 T cells
CD8 T cells
CART
non-CART
D
Simpson's Index of Diversity (1-D)
E
Cytotoxicity
Exhaustion
Term. Exhaustion
AU
F
TIM-3
PD-1
4.88
6.03
17.2

Figure 5. Reshaping of T cells to a favorable state for anti-cancer immunity in G36-PDL1

(A) UMAP plot of RNA velocity for $CD8^+$ T cells in G36-PDL1 (left panel). Heatmap of transition ratio from cell types in column to cell types in row (middle panel). Heatmap of mean signature score of cytotoxicity in G36-PDL1 (right panel).

(B) UMAP plot of clonal expansion in each group (multiplet in red, singlet in cyan).

(C) Heatmap of multiplet ratio in all the T cells, $CD4^+$ T cells, and $CD8^+$ T cells from each group (left). Heatmap of multiplet ratio in all the T cells, CAR-seq expressing T cells, or non-CAR-seq expressing T cells from each group (right). White color indicates no value.

(D) Heatmap of Simpson's Index of Diversity (1-D) in all the T cells, $CD4^+$ T cells, and $CD8^+$ T cells from each group.

(E) Violin plot of a given signature between groups. * indicates p value <0.05.

(F) Percentage of terminally exhausted T cells ($PD1^{hi}$ $TIM\text{-}3^+$) in tumor-infiltrating T cells of G36-PDL1 (pink), G36-SARS (orange), A716-PDL1 (blue) groups.

this hccRCC-NSG-SGM3 mouse model. CAR-T cells with target recognition and PD-L1 mAb were superior to either alone, i.e., G36-PDL1 CAR-T cells that secreted PD-L1 mAb exhibited superior tumor inhibition compared to G36-SARS or A716-PDL1. This increase in G36-PDL1 CAR-T cell therapeutic effect *in vivo* is likely due to multiple factors including their increased cytotoxicity, resistance to exhaustion, and their ability to change the TME by decreasing communication among exhausted T cells and M2-like macrophages and enhancing Tfh-B cell crosstalk.

Previous studies have demonstrated that the absence of human immunity in mouse models compromises their value in translational research and the development of novel immuno-oncology therapies.[67,68] The construction of humanized animal models has allowed for the development of a rudimentary level of innate and adaptive human immunity in mice.[69] The NSG-SGM3 strain expressing human stem cell factor, GM-CSF, and IL-3 transgenes is a superior mouse model for humanization to assess immunotherapies and to study the TME.[70,71] NSG-SGM3 strain shows the most efficient engraftment of HSCs to date as well as marked improvement in development of myeloid cells following HSC engraftment *in vivo*[72–75] thereby serving as an ideal tool for studying myeloid cell crosstalk. Here, to achieve high humanization efficiency, we humanized NSG-SGM3 mouse with fetal tissue as it has been reported that transferring fetal liver or cord blood-derived HSCs results in a higher engraftment of human $CD45^+$ cells compared to engrafting the bone marrow or mobilized peripheral blood derived HSCs.[76,77] In addition, we engrafted newborns as they exhibited a better reconstitution of human $CD45^+$ cells compared to adult recipients.[75,78,79] To avoid graft-versus-host disease and nonspecific tumor killing, we used HSCs that were partially HLA matched to the tumor. The humanization and the corresponding immune response are dynamic, with high B cell reconstitution and low T cell reconstitution at the early stage (less than 10 weeks after reconstitution), and then significant T cell expansion at the later stage (around week 30).[80] In our hccRCC-NSG-SGM3 mouse model, we observed a similar trend and started the experiment at circa 70% T cell percentage (Figure S1C) which is similar to the percentage of circulating T cells in human peripheral leukocytes.[81]

The lack of clinically relevant models for testing human immunotherapy hinders the development of cancer therapies. This is also true for ccRCC, where existing *in vivo* models poorly recapitulate the TME.[82] For example, traditional mouse models of renal cancer poorly represent human immune cells since some members of the B7 immune checkpoint family, including HHLA2 which is highly expressed in kidney cancer,[83,84] have no mouse ortholog.[85]

Previous studies in tumor-bearing HuNSG mice have shown that both $CD4^+$ and $CD8^+$ T cell clones recovered from tumor-bearing mice demonstrated HLA-restricted tumor cell killing[75] and antitumor responses with pembrolizumab treatment.[28] In addition, human thymopoiesis within the mouse thymus has been shown to occur,[28] and education could be further improved by rectifying restrictions in cross-species HLA-dependent antigen-specific immune responses.[86] Here, we further advanced the humanized mouse models by profiling the TME of treatment naive at baseline (Figure S4) and in all treatment groups (Figures 3D and 3E), demonstrating that hccRCC-NSG-SGM3 is able to reconstitute most types of human ccRCC patient TILs, thus, providing a promising tool for preclinical evaluation of immunotherapies and studying TME. To study the human antigen-specific response, we studied CD39 (*ENTPD1*)-positive tumor-infiltrating T cells as CD39 is highly expressed in tumor-specific $CD8^+$ TILs but not bystander TILs.[60] We found CD39 expression in all $CD8^+$ T cell subsets, indicating a general tumor-specific response in hccRCC-NSG-SGM3 mouse model (Figure S7D).

This IR CAR-T strategy showed that a secreted anti-PD-L1 mAb can work *in trans* to reverse exhaustion of TILs, a significant advantage over CAR-T cells that use CRISPR to knock out PD-1 expression, which only prevents this checkpoint activity in the CAR-T cells,[87,88] but cannot reverse exhaustion of endogenous T cells or myeloid cells.[89] Moreover, deletion of PDCD1 has been reported to impair T cell survival, memory development, and function.[90] This cell-based combination immunotherapy is formulated to be administered as one single agent which should also restrict effects of the ICI mainly to the tumor site and mitigate against the side effects caused by systematically administrated ICIs.[91,92]

In the ccRCC TME, M2 macrophages and exhausted $CD8^+$ T cells form a bidirectional circuit where exhausted T cells express high inhibitory checkpoint molecules (PD-1, CTLA-4, TIGIT, LAG-3) and produce M2 modulators (CSF1, MIF) to promote M2 polarization, while M2-like macrophages highly express the corresponding ligands and receptors (PD-L1/2, CD86, PVR, CSF1R, CD74) to facilitate T cell exhaustion.[18,19] Our data support that G36-PDL1 CAR-T cells were able to interrupt this dysfunctional regulation and rewire TME with higher cytotoxic $CD8^+$ T infiltration and lower M2 infiltration by downregulating the crosstalk between $CD8^+$ T and M2 as well as downregulating the negative regulators (Figures 3F, 3G, and 6D; Table S10).

In summary, the hccRCC-NSG-SGM3 is able to model advanced ccRCC TME and provides a powerful tool for ccRCC TME study and immunotherapy assessment. Anti-CAIX G36-PDL1 IR CAR-T cells secreting anti-PD-L1 mAb exhibited superior tumor control and successfully restored active antitumor immunity in the hccRCC-NSG-SGM3 model. This treatment holds promise to achieve ccRCC cures by rewiring local TME.

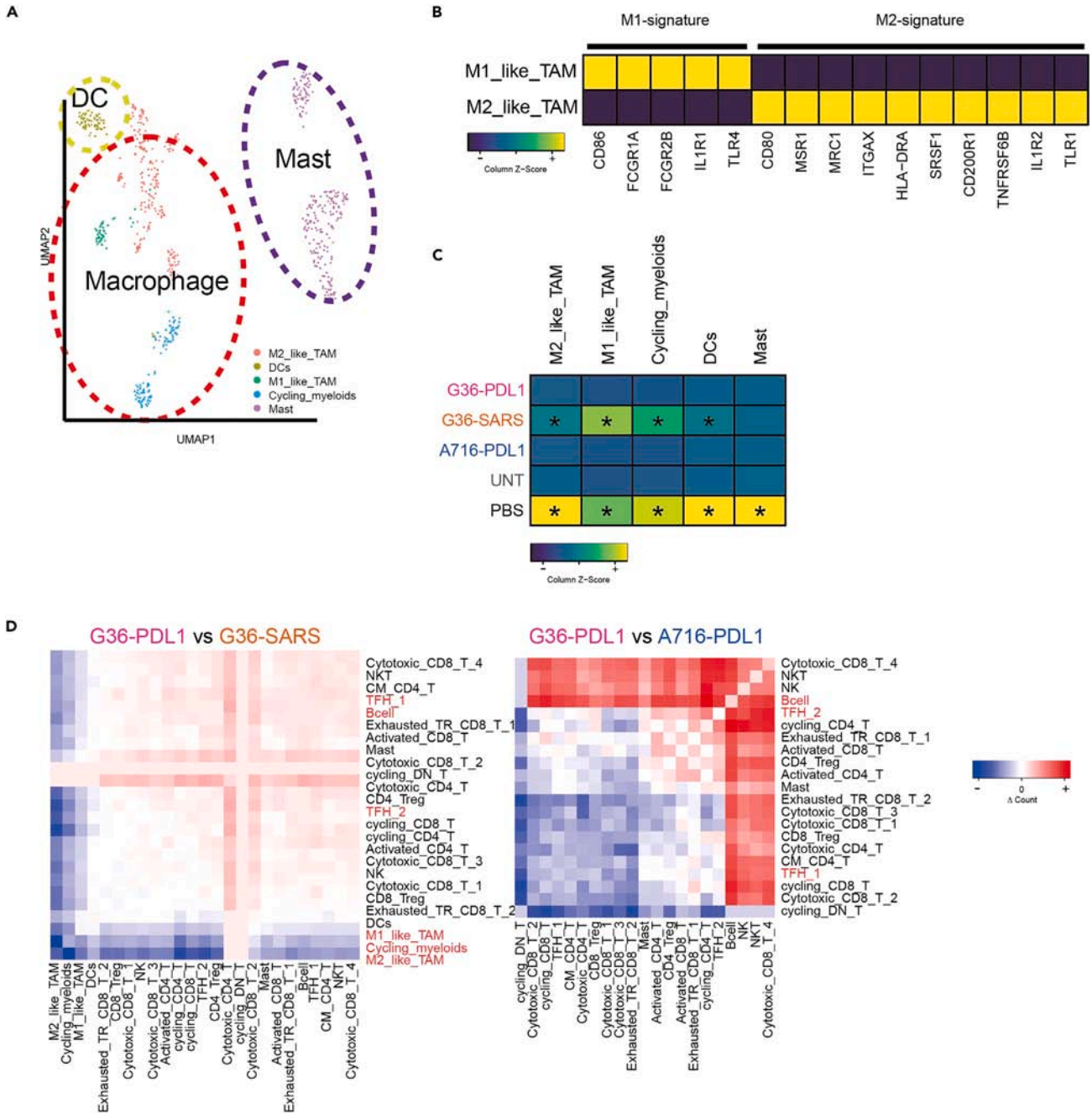

Figure 6. TME in G36-PDL1 has been reshaped into a preferable environment for anti-cancer effect

(A) UMAP plot of myeloid subsets.

(B) Heatmap of M1 and M2 macrophage signature gene in M1_like_TAM and M2_like_TAM.

(C) Heatmap of relative cell abundance of myeloid subsets out of total TILs between groups. * indicates a significant difference (fold change >2, q value <0.01) comparing to G36-PDL1.

(D) The difference of cell-cell interaction counts between two groups from CellChat package. The positive (red) sign indicates a higher value from G36-PDL1 comparing to G36-SARS (left panel) and to A716-PDL1 (right panel).

Limitations of the study

Potential limitations of our study include limited animal numbers, lack of analysis of neutrophils, and other immune components which are sensitive to degradation and have relatively low RNA content.[93,94] The lack of human HLA class I and II in the thymus of the humanized mouse

model can be improved using Thy/HSC,[95] BLT,[96] and human HLA gene-expressing[86] models to generate HLA-restricted antigen-specific human T cell reactions. To further study the dynamics of humanization, scRNA-seq of samples collected at different time points should be performed. Mouse PD-L1 was reported to negatively signal human PD-1,[97] thus the cross reactivity needs to be further investigated in this humanized mouse model. Previous study has shown that in a xenograft mouse model of metastatic ovarian tumor, mice treated with CAR-T cells secreting anti-PD-1 scFv had enhanced survival benefit over mice treated with CAR-T cells and systemic administration of anti-PD-1 mAb, so that we did not include systemic anti-PD-L1 mAb as a control in our experimental design.[94] Additionally in the future, due to the high conservation between human and murine CXCR4 and CXCL12, we will include mouse fibroblasts to comprehensively study the TME.[98] Finally, additional animal models and experimental efforts are needed to have a better understanding of the enhanced Tfh-B crosstalk that was observed in the G36-PDL1 TME.

STAR★METHODS

Detailed methods are provided in the online version of this paper and include the following:

- KEY RESOURCES TABLE
- RESOURCE AVAILABILITY
  - Lead contact
  - Materials availability
  - Data and code availability
- EXPERIMENTAL MODEL AND STUDY PARTICIPANT DETAILS
  - Cell lines and culture
  - Ethical approval
- METHODS DETAILS
  - Production of lentivirus particles
  - Generation of CAR-T cells
  - Payload quantification
  - HLA typing
  - *In vitro* killing assay
  - Flow cytometry
  - *In vivo* orthotopic humanized ccRCC model
  - Bioluminescence imaging (BLI)
  - Tumor dissociation and tumor infiltrating CAR-T cell isolation
  - RNA-seq 10X genomics library preparation, hash tag, and single cell 5′ sequencing
  - Data processing
  - Merging and batch correction of main celltypes
  - Subclustering of myeloid and T cells
  - Data transferring to human ccRCC data
  - T cell clonality analysis
  - Cell abundance analysis
  - Signature analysis
  - DEG analysis between groups
  - Cell-cell interaction analysis
  - RNA velocity analysis
- QUANTIFICATION AND STATISTICAL ANALYSIS

SUPPLEMENTAL INFORMATION

Supplemental information can be found online at https://doi.org/10.1016/j.isci.2024.108879.

ACKNOWLEDGMENTS

This work was supported by the Assistant Secretary of Defense for Health Affairs endorsed by the Department of Defense, through the FY21 Translational Research Partnership Award (W81XWH-21-1-0442) and FY21 Idea Development Award (W81XWH-21-1-0482) to W.A.M. Opinions, interpretations, conclusions, and recommendations are those of the authors and are not necessarily endorsed by the Department of Defense. This work was partially supported by NCI P50CA101942 to G.J.F. This work was also supported by the Wong Family Award and KCA Trailblazer Award to Y.W. In addition, J.W.C. and M.H. were funded by the Evergrande Center and the Helmsley Foundation (2008-04050). K.W. is supported by a Burroughs Wellcome Fund Career Awards for Medical Scientists, a Doris Duke Charitable Foundation Clinical Scientist Development Award, and a Rheumatology Research Foundation Innovative Research Award. D.A.B. is in part supported by the DOD CDMRP Academy of Kidney Cancer Investigators (KC190128). T.K.C. is supported in part by the Dana-Farber/Harvard Cancer Center Kidney

SPORE (2P50CA101942-16) and Program 5P30CA006516-56, the Kohlberg Chair at Harvard Medical School and the Trust Family, Michael Brigham, Pan Mass Challenge, and Loker Pinard Funds for Kidney Cancer Research at DFCI.

AUTHOR CONTRIBUTIONS

Y.W. and W.A.M. designed the study. Y.W., J.-W.C., G.K., A.B., C.R., A.C.C., J.S., K.J., Q.-D.N., and Z.Z. performed the experiments. Y.W., J.-W.C., G.K., A.C.C., and M.H. analyzed the data. Y.W., J.-W.C., G.K., M.H., G.J.F., and W.A.M. wrote the manuscript. Y.W., J.-W.C., G.K., A.B., C.R., A.C.C., J.S., D.A.B., T.K.C., C.J.W., K.J., Q.-D.N., Z.Z., K.W., Q.Z., S.S., G.J.F., M.H., and W.A.M. edited and approved the manuscript.

DECLARATION OF INTERESTS

W.A.M. has patents in the PD-1/PDL1 field. G.J.F. has patents/pending royalties on the PD-1/PD-L1 pathway from Roche, Merck MSD, Bristol-Myers-Squibb, Merck KGA, Boehringer-Ingelheim, AstraZeneca, Dako, Leica, Mayo Clinic, Eli Lilly, and Novartis. G.J.F. has served on advisory boards for Roche, Bristol-Myers-Squibb, Xios, Origimed, Triursus, iTeos, NextPoint, IgM, Jubilant, Trillium, IOME, GV20, Invaria, and Geode. G.J.F. has equity in NextPoint, Triursus, Xios, iTeos, IgM, GV20, Invaria, and Geode. M.H. is a co-founder of Neomer Diagnostics where he is also on the advisory board. K.W. received a sponsored-research agreement from Gilead Sciences. K.W. served as a consultant for Gilead Sciences and Horizon Therapeutics. D.A.B. reports nonfinancial support from Bristol Myers Squibb, honoraria from LM Education/Exchange Services, advisory board fees from Exelixis and AVEO, personal fees from Charles River Associates, Schlesinger Associates, Imprint Science, Insight Strategy, Trinity Group, Cancer Expert Now, Adnovate Strategies, MDedge, CancerNetwork, Catenion, OncLive, Cello Health BioConsulting, PWW Consulting, Haymarket Medical Network, Aptitude Health, ASCO Post/Harborside, Targeted Oncology, and AbbVie, and research support from Exelixis and AstraZeneca, outside of the submitted work. C.J.W. holds equity in BioNTech, Inc., and receives research funding from Pharmacyclics. S.S. reports receiving commercial research grants from Bristol-Myers Squibb, AstraZeneca, Exelixis, and Novartis; is a consultant/advisory board member for Merck, AstraZeneca, Bristol-Myers Squibb, CRISPR Therapeutics AG, AACR, and NCI; receives royalties from Biogenex; and mentored several non-US citizens on research projects with potential funding (in part) from non-US sources/Foreign Components. T.K.C. reports institutional and personal, paid and unpaid support for research, advisory boards, consultancy, and honoraria from AstraZeneca, Aravive, Aveo, Bayer, Bristol Myers-Squibb, Calithera, Circle Pharma, Eisai, EMD Serono, Exelixis, GlaxoSmithKline, IQVA, Infinity, Ipsen, Jansen, Kanaph, Lilly, Merck, Nikang, Nuscan, Novartis, Pfizer, Roche, Sanofi/Aventis, Surface Oncology, Takeda, Tempest, Up-To-Date, and CME events (Peerview, OncLive, MJH, and others), outside the submitted work. T.K.C. has institutional patents filed on molecular alterations and immunotherapy response/toxicity, and ctDNA. T.K.C. has equity in Tempest, Pionyr, Osel, and Precede Bio. T.K.C. has served on committees for NCCN, GU Steering Committee, ASCO/ESMO, ACCRU, and KidneyCan. T.K.C. has medical writing and editorial assistance support may have been funded by Communications companies in part. T.K.C. has mentored several non-US citizens on research projects with potential funding (in part) from non-US sources/Foreign Components. The institution (Dana-Farber Cancer Institute) may have received additional independent funding of drug companies or/and royalties potentially involved in research around the subject matter.

Received: October 12, 2023
Revised: December 1, 2023
Accepted: January 8, 2024
Published: January 15, 2024

REFERENCES

1. Maude, S.L., Laetsch, T.W., Buechner, J., Rives, S., Boyer, M., Bittencourt, H., Bader, P., Verneris, M.R., Stefanski, H.E., Myers, G.D., et al. (2018). Tisagenlecleucel in Children and Young Adults with B-Cell Lymphoblastic Leukemia. N. Engl. J. Med. *378*, 439–448.
2. Schuster, S.J., Bishop, M.R., Tam, C.S., Waller, E.K., Borchmann, P., McGuirk, J.P., Jäger, U., Jaglowski, S., Andreadis, C., Westin, J.R., et al. (2019). Tisagenlecleucel in Adult Relapsed or Refractory Diffuse Large B-Cell Lymphoma. N. Engl. J. Med. *380*, 45–56.
3. Wang, M., Munoz, J., Goy, A., Locke, F.L., Jacobson, C.A., Hill, B.T., Timmerman, J.M., Holmes, H., Jaglowski, S., Flinn, I.W., et al. (2020). KTE-X19 CAR T-Cell Therapy in Relapsed or Refractory Mantle-Cell Lymphoma. N. Engl. J. Med. *382*, 1331–1342.
4. Abramson, J.S., Palomba, M.L., Gordon, L.I., Lunning, M.A., Wang, M., Arnason, J., Mehta, A., Purev, E., Maloney, D.G., Andreadis, C., et al. (2020). Lisocabtagene maraleucel for patients with relapsed or refractory large B-cell lymphomas (TRANSCEND NHL 001): a multicentre seamless design study. Lancet *396*, 839–852.
5. Neelapu, S.S., Locke, F.L., Bartlett, N.L., Lekakis, L.J., Miklos, D.B., Jacobson, C.A., Braunschweig, I., Oluwole, O.O., Siddiqi, T., Lin, Y., et al. (2017). Axicabtagene Ciloleucel CAR T-Cell Therapy in Refractory Large B-Cell Lymphoma. N. Engl. J. Med. *377*, 2531–2544.
6. Locke, F.L., Ghobadi, A., Jacobson, C.A., Miklos, D.B., Lekakis, L.J., Oluwole, O.O., Lin, Y., Braunschweig, I., Hill, B.T., Timmerman, J.M., et al. (2019). Long-term safety and activity of axicabtagene ciloleucel in refractory large B-cell lymphoma (ZUMA-1): a single-arm, multicentre, phase 1-2 trial. Lancet Oncol. *20*, 31–42.
7. FDA Approves First Cell-Based Gene Therapy for Adult Patients with Multiple Myeloma. https://www.fda.gov/news-events/press-announcements/fda-approves-first-cell-based-gene-therapy-adult-patients-multiple-myeloma.
8. Berdeja, J.G., Madduri, D., Usmani, S.Z., Jakubowiak, A., Agha, M., Cohen, A.D., Stewart, A.K., Hari, P., Htut, M., Lesokhin, A., et al. (2021). Ciltacabtagene autoleucel, a B-cell maturation antigen-directed chimeric antigen receptor T-cell therapy in patients with relapsed or refractory multiple myeloma (CARTITUDE-1): a phase 1b/2 open-label study. Lancet *398*, 314–324.
9. Tahmasebi, S., Elahi, R., and Esmaeilzadeh, A. (2019). Solid Tumors Challenges and New

Insights of CAR T Cell Engineering. Stem Cell Rev. Rep. *15*, 619–636.
10. Leko, V., and Rosenberg, S.A. (2020). Identifying and Targeting Human Tumor Antigens for T Cell-Based Immunotherapy of Solid Tumors. Cancer Cell *38*, 454–472.
11. Rafiq, S., Hackett, C.S., and Brentjens, R.J. (2020). Engineering strategies to overcome the current roadblocks in CAR T cell therapy. Nat. Rev. Clin. Oncol. *17*, 147–167.
12. Wang, Y., Suarez, E.R., Kastrunes, G., de Campos, N.S.P., Abbas, R., Pivetta, R.S., Murugan, N., Chalbatani, G.M., D'Andrea, V., and Marasco, W.A. (2024). Evolution of cell therapy for renal cell carcinoma. Mol. Cancer *23*, 8.
13. Kakarla, S., and Gottschalk, S. (2014). CAR T cells for solid tumors: armed and ready to go? Cancer J. *20*, 151–155.
14. Fridman, W.H., Zitvogel, L., Sautès-Fridman, C., and Kroemer, G. (2017). The immune contexture in cancer prognosis and treatment. Nat. Rev. Clin. Oncol. *14*, 717–734.
15. Binnewies, M., Roberts, E.W., Kersten, K., Chan, V., Fearon, D.F., Merad, M., Coussens, L.M., Gabrilovich, D.I., Ostrand-Rosenberg, S., Hedrick, C.C., et al. (2018). Understanding the tumor immune microenvironment (TIME) for effective therapy. Nat. Med. *24*, 541–550.
16. Chevrier, S., Levine, J.H., Zanotelli, V.R.T., Silina, K., Schulz, D., Bacac, M., Ries, C.H., Ailles, L., Jewett, M.A.S., Moch, H., et al. (2017). An Immune Atlas of Clear Cell Renal Cell Carcinoma. Cell *169*, 736–749.e18.
17. Braun, D.A., Hou, Y., Bakouny, Z., Ficial, M., Sant' Angelo, M., Forman, J., Ross-Macdonald, P., Berger, A.C., Jegede, O.A., Elagina, L., et al. (2020). Interplay of somatic alterations and immune infiltration modulates response to PD-1 blockade in advanced clear cell renal cell carcinoma. Nat. Med. *26*, 909–918.
18. Bi, K., He, M.X., Bakouny, Z., Kanodia, A., Napolitano, S., Wu, J., Grimaldi, G., Braun, D.A., Cuoco, M.S., Mayorga, A., et al. (2021). Tumor and immune reprogramming during immunotherapy in advanced renal cell carcinoma. Cancer Cell *39*, 649–661.e5.
19. Braun, D.A., Street, K., Burke, K.P., Cookmeyer, D.L., Denize, T., Pedersen, C.B., Gohil, S.H., Schindler, N., Pomerance, L., Hirsch, L., et al. (2021). Progressive immune dysfunction with advancing disease stage in renal cell carcinoma. Cancer Cell *39*, 632–648.e8.
20. Zheng, C., Zheng, L., Yoo, J.K., Guo, H., Zhang, Y., Guo, X., Kang, B., Hu, R., Huang, J.Y., Zhang, Q., et al. (2017). Landscape of Infiltrating T Cells in Liver Cancer Revealed by Single-Cell Sequencing. Cell *169*, 1342–1356.e16.
21. Zhang, Y., Chen, H., Mo, H., Hu, X., Gao, R., Zhao, Y., Liu, B., Niu, L., Sun, X., Yu, X., et al. (2021). Single-cell analyses reveal key immune cell subsets associated with response to PD-L1 blockade in triple-negative breast cancer. Cancer Cell *39*, 1578–1593.e8.
22. Zhang, L., Li, Z., Skrzypczynska, K.M., Fang, Q., Zhang, W., O'Brien, S.A., He, Y., Wang, L., Zhang, Q., Kim, A., et al. (2020). Single-Cell Analyses Inform Mechanisms of Myeloid-Targeted Therapies in Colon Cancer. Cell *181*, 442–459.e29.
23. Cho, H., Du, X., Rizzi, J.P., Liberzon, E., Chakraborty, A.A., Gao, W., Carvo, I., Signoretti, S., Bruick, R.K., Josey, J.A., et al. (2016). On-target efficacy of a HIF-2α antagonist in preclinical kidney cancer models. Nature *539*, 107–111.
24. Gu, Y.F., Cohn, S., Christie, A., McKenzie, T., Wolff, N., Do, Q.N., Madhuranthakam, A.J., Pedrosa, I., Wang, T., Dey, A., et al. (2017). Modeling Renal Cell Carcinoma in Mice: Bap1 and Pbrm1 Inactivation Drive Tumor Grade. Cancer Discov. *7*, 900–917.
25. Gonzalez, L., Strbo, N., and Podack, E.R. (2013). Humanized mice: novel model for studying mechanisms of human immune-based therapies. Immunol. Res. *57*, 326–334.
26. Chuprin, J., Buettner, H., Seedhom, M.O., Greiner, D.L., Keck, J.G., Ishikawa, F., Shultz, L.D., and Brehm, M.A. (2023). Humanized mouse models for immuno-oncology research. Nat. Rev. Clin. Oncol. *20*, 192–206.
27. Wang, Y., Shelton, S.E., Kastrunes, G., Barbie, D.A., Freeman, G.J., and Marasco, W.A. (2022). Preclinical models for development of immune–oncology therapies. Immuno-oncol. Insights *3*, 379–398.
28. Wang, M., Yao, L.C., Cheng, M., Cai, D., Martinek, J., Pan, C.X., Shi, W., Ma, A.H., De Vere White, R.W., Airhart, S., et al. (2018). Humanized mice in studying efficacy and mechanisms of PD-1-targeted cancer immunotherapy. Faseb j *32*, 1537–1549.
29. Zhao, Y., Shuen, T.W.H., Toh, T.B., Chan, X.Y., Liu, M., Tan, S.Y., Fan, Y., Yang, H., Lyer, S.G., Bonney, G.K., et al. (2018). Development of a new patient-derived xenograft humanised mouse model to study human-specific tumour microenvironment and immunotherapy. Gut *67*, 1845–1854.
30. Suarez, E.R., Chang, D.K., Sun, J., Sui, J., Freeman, G.J., Signoretti, S., Zhu, Q., and Marasco, W.A. (2016). Chimeric antigen receptor T cells secreting anti-PD-L1 antibodies more effectively regress renal cell carcinoma in a humanized mouse model. Oncotarget *7*, 34341–34355.
31. Wang, Y., Buck, A., Grimaud, M., Culhane, A.C., Kodangattil, S., Razimbaud, C., Bonal, D.M., Nguyen, Q.D., Zhu, Z., Wei, K., et al. (2022). Anti-CAIX BBζ CAR4/8 T cells exhibit superior efficacy in a ccRCC mouse model. Mol. Ther. Oncolytics *24*, 385–399.
32. Shen, C., and Kaelin, W.G., Jr. (2013). The VHL/HIF axis in clear cell renal carcinoma. Semin. Cancer Biol. *23*, 18–25.
33. Ruf, M., Mittmann, C., Nowicka, A.M., Hartmann, A., Hermanns, T., Poyet, C., van den Broek, M., Sulser, T., Moch, H., and Schraml, P. (2015). pVHL/HIF-regulated CD70 expression is associated with infiltration of CD27+ lymphocytes and increased serum levels of soluble CD27 in clear cell renal cell carcinoma. Clin. Cancer Res. *21*, 889–898.
34. Xu, C., Lo, A., Yammanuru, A., Tallarico, A.S.C., Brady, K., Murakami, A., Barteneva, N., Zhu, Q., and Marasco, W.A. (2010). Unique biological properties of catalytic domain directed human anti-CAIX antibodies discovered through phage-display technology. PLoS One *5*, e9625.
35. Chang, D.K., Moniz, R.J., Xu, Z., Sun, J., Signoretti, S., Zhu, Q., and Marasco, W.A. (2015). Human anti-CAIX antibodies mediate immune cell inhibition of renal cell carcinoma in vitro and in a humanized mouse model in vivo. Mol. Cancer *14*, 119.
36. Lo, A.S.Y., Xu, C., Murakami, A., and Marasco, W.A. (2014). Regression of established renal cell carcinoma in nude mice using lentivirus-transduced human T cells expressing a human anti-CAIX chimeric antigen receptor. Mol. Ther. Oncolytics *1*, 14003.
37. Silva, J.P., Vetterlein, O., Jose, J., Peters, S., and Kirby, H. (2015). The S228P mutation prevents in vivo and in vitro IgG4 Fab-arm exchange as demonstrated using a combination of novel quantitative immunoassays and physiological matrix preparation. J. Biol. Chem. *290*, 5462–5469.
38. Wang, Y., Chan, L.L., Grimaud, M., Fayed, A., Zhu, Q., and Marasco, W.A. (2020). High-Throughput Image Cytometry Detection Method for CAR-T Transduction, Cell Proliferation, and Cytotoxicity Assays. Cytometry *99*, 689–697.
39. Dhupkar, P., Gordon, N., Stewart, J., and Kleinerman, E.S. (2018). Anti-PD-1 therapy redirects macrophages from an M2 to an M1 phenotype inducing regression of OS lung metastases. Cancer Med. *7*, 2654–2664.
40. Yamaguchi, Y., Gibson, J., Ou, K., Lopez, L.S., Ng, R.H., Leggett, N., Jonsson, V.D., Zarif, J.C., Lee, P.P., Wang, X., et al. (2022). PD-L1 blockade restores CAR T cell activity through IFN-gamma-regulation of CD163+ M2 macrophages. J. Immunother. Cancer *10*, e004400.
41. Yang, F., Zhao, J., Luo, X., Li, T., Wang, Z., Wei, Q., Lu, H., Meng, Y., Cai, K., Lu, L., et al. (2021). Transcriptome Profiling Reveals B-Lineage Cells Contribute to the Poor Prognosis and Metastasis of Clear Cell Renal Cell Carcinoma. Front. Oncol. *11*, 731896.
42. Li, S., Huang, C., Hu, G., Ma, J., Chen, Y., Zhang, J., Huang, Y., Zheng, J., Xue, W., Xu, Y., and Zhai, W. (2020). Tumor-educated B cells promote renal cancer metastasis via inducing the IL-1β/HIF-2α/Notch1 signals. Cell Death Dis. *11*, 163.
43. Meylan, M., Petitprez, F., Becht, E., Bougoüin, A., Pupier, G., Calvez, A., Giglioli, I., Verkarre, V., Lacroix, G., Verneau, J., et al. (2022). Tertiary lymphoid structures generate and propagate anti-tumor antibody-producing plasma cells in renal cell cancer. Immunity *55*, 527–541.e5.
44. Italiano, A., Bessede, A., Pulido, M., Bompas, E., Piperno-Neumann, S., Chevreau, C., Penel, N., Bertucci, F., Toulmonde, M., Bellera, C., et al. (2022). Pembrolizumab in soft-tissue sarcomas with tertiary lymphoid structures: a phase 2 PEMBROSARC trial cohort. Nat. Med. *28*, 1199–1206.
45. Cho, J.W., Park, S., Kim, G., Han, H., Shim, H.S., Shin, S., Bae, Y.S., Park, S.Y., Ha, S.J., Lee, I., and Kim, H.R. (2021). Dysregulation of TFH-B-TRM lymphocyte cooperation is associated with unfavorable anti-PD-1 responses in EGFR-mutant lung cancer. Nat. Commun. *12*, 6068.
46. Crotty, S. (2011). Follicular helper CD4 T cells (TFH). Annu. Rev. Immunol. *29*, 621–663.
47. Gu-Trantien, C., Migliori, E., Buisseret, L., de Wind, A., Brohée, S., Garaud, S., Noël, G., Dang Chi, V.L., Lodewyckx, J.N., Naveaux, C., et al. (2017). CXCL13-producing TFH cells link immune suppression and adaptive memory in human breast cancer. JCI Insight *2*, e91487.
48. Flemming, A. (2021). GZMK(+) T cells a hallmark of immune ageing. Nat. Rev. Immunol. *21*, 1.
49. Mogilenko, D.A., Shpynov, O., Andhey, P.S., Arthur, L., Swain, A., Esaulova, E., Brioschi, S., Shchukina, I., Kerndl, M., Bambouskova, M., et al. (2021). Comprehensive Profiling of

an Aging Immune System Reveals Clonal GZMK(+) CD8(+) T Cells as Conserved Hallmark of Inflammaging. Immunity *54*, 99–115.e12.
50. La Manno, G., Soldatov, R., Zeisel, A., Braun, E., Hochgerner, H., Petukhov, V., Lidschreiber, K., Kastriti, M.E., Lönnerberg, P., Furlan, A., et al. (2018). RNA velocity of single cells. Nature *560*, 494–498.
51. Mishra, S., Srinivasan, S., Ma, C., and Zhang, N. (2021). CD8(+) Regulatory T Cell - A Mystery to Be Revealed. Front. Immunol. *12*, 708874.
52. Churlaud, G., Pitoiset, F., Jebbawi, F., Lorenzon, R., Bellier, B., Rosenzwajg, M., and Klatzmann, D. (2015). Human and Mouse CD8(+)CD25(+)FOXP3(+) Regulatory T Cells at Steady State and during Interleukin-2 Therapy. Front. Immunol. *6*, 171.
53. Zhulai, G., and Oleinik, E. (2022). Targeting regulatory T cells in anti-PD-1/PD-L1 cancer immunotherapy. Scand. J. Immunol. *95*, e13129.
54. Plitas, G., Konopacki, C., Wu, K., Bos, P.D., Morrow, M., Putintseva, E.V., Chudakov, D.M., and Rudensky, A.Y. (2016). Regulatory T Cells Exhibit Distinct Features in Human Breast Cancer. Immunity *45*, 1122–1134.
55. Tong, A.A., Forestell, B., Murphy, D.V., Nair, A., Allen, F., Myers, J., Klauschen, F., Shen, C., Gopal, A.A., Huang, A.Y., and Mandl, J.N. (2019). Regulatory T cells differ from conventional CD4(+) T cells in their recirculatory behavior and lymph node transit times. Immunol. Cell Biol. *97*, 787–798.
56. Francisco, L.M., Salinas, V.H., Brown, K.E., Vanguri, V.K., Freeman, G.J., Kuchroo, V.K., and Sharpe, A.H. (2009). PD-L1 regulates the development, maintenance, and function of induced regulatory T cells. J. Exp. Med. *206*, 3015–3029.
57. Valpione, S., Mundra, P.A., Galvani, E., Campana, L.G., Lorigan, P., De Rosa, F., Gupta, A., Weightman, J., Mills, S., Dhomen, N., and Marais, R. (2021). The T cell receptor repertoire of tumor infiltrating T cells is predictive and prognostic for cancer survival. Nat. Commun. *12*, 4098.
58. Valpione, S., Galvani, E., Tweedy, J., Mundra, P.A., Banyard, A., Middlehurst, P., Barry, J., Mills, S., Salih, Z., Weightman, J., et al. (2020). Immune awakening revealed by peripheral T cell dynamics after one cycle of immunotherapy. Nat. Cancer *1*, 210–221.
59. Kato, T., Kiyotani, K., Tomiyama, E., Koh, Y., Matsushita, M., Hayashi, Y., Nakano, K., Ishizuya, Y., Wang, C., Hatano, K., et al. (2021). Peripheral T cell receptor repertoire features predict durable responses to anti-PD-1 inhibitor monotherapy in advanced renal cell carcinoma. OncoImmunology *10*, 1862948.
60. Simoni, Y., Becht, E., Fehlings, M., Loh, C.Y., Koo, S.-L., Teng, K.W.W., Yeong, J.P.S., Nahar, R., Zhang, T., Kared, H., et al. (2018). Bystander CD8+ T cells are abundant and phenotypically distinct in human tumour infiltrates. Nature *557*, 575–579.
61. Jin, H.T., Anderson, A.C., Tan, W.G., West, E.E., Ha, S.J., Araki, K., Freeman, G.J., Kuchroo, V.K., and Ahmed, R. (2010). Cooperation of Tim-3 and PD-1 in CD8 T-cell exhaustion during chronic viral infection. Proc. Natl. Acad. Sci. USA *107*, 14733–14738.
62. Sen, D.R., Kaminski, J., Barnitz, R.A., Kurachi, M., Gerdemann, U., Yates, K.B., Tsao, H.W., Godec, J., LaFleur, M.W., Brown, F.D., et al. (2016). The epigenetic landscape of T cell exhaustion. Science *354*, 1165–1169.
63. Duan, Z., and Luo, Y. (2021). Targeting macrophages in cancer immunotherapy. Signal Transduct. Target. Ther. *6*, 127.
64. Jin, S., Guerrero-Juarez, C.F., Zhang, L., Chang, I., Ramos, R., Kuan, C.H., Myung, P., Plikus, M.V., and Nie, Q. (2021). Inference and analysis of cell-cell communication using CellChat. Nat. Commun. *12*, 1088.
65. Roger, T., David, J., Glauser, M.P., and Calandra, T. (2001). MIF regulates innate immune responses through modulation of Toll-like receptor 4. Nature *414*, 920–924.
66. Stanley, E.R., and Chitu, V. (2014). CSF-1 receptor signaling in myeloid cells. Cold Spring Harb. Perspect. Biol. *6*, a021857.
67. Aparicio, S., Hidalgo, M., and Kung, A.L. (2015). Examining the utility of patient-derived xenograft mouse models. Nat. Rev. Cancer *15*, 311–316.
68. Tian, H., Lyu, Y., Yang, Y.G., and Hu, Z. (2020). Humanized Rodent Models for Cancer Research. Front. Oncol. *10*, 1696.
69. Brehm, M.A., Cuthbert, A., Yang, C., Miller, D.M., DiIorio, P., Laning, J., Burzenski, L., Gott, B., Foreman, O., Kavirayani, A., et al. (2010). Parameters for establishing humanized mouse models to study human immunity: analysis of human hematopoietic stem cell engraftment in three immunodeficient strains of mice bearing the IL2rgamma(null) mutation. Clin. Immunol. *135*, 84–98.
70. Shultz, L.D., Brehm, M.A., Garcia-Martinez, J.V., and Greiner, D.L. (2012). Humanized mice for immune system investigation: progress, promise and challenges. Nat. Rev. Immunol. *12*, 786–798.
71. Morton, J.J., Bird, G., Refaeli, Y., and Jimeno, A. (2016). Humanized Mouse Xenograft Models: Narrowing the Tumor-Microenvironment Gap. Cancer Res. *76*, 6153–6158.
72. Nicolini, F.E., Cashman, J.D., Hogge, D.E., Humphries, R.K., and Eaves, C.J. (2004). NOD/SCID mice engineered to express human IL-3, GM-CSF and Steel factor constitutively mobilize engrafted human progenitors and compromise human stem cell regeneration. Leukemia *18*, 341–347.
73. Wunderlich, M., Chou, F.S., Link, K.A., Mizukawa, B., Perry, R.L., Carroll, M., and Mulloy, J.C. (2010). AML xenograft efficiency is significantly improved in NOD/SCID-IL2RG mice constitutively expressing human SCF, GM-CSF and IL-3. Leukemia *24*, 1785–1788.
74. Jangalwe, S., Shultz, L.D., Mathew, A., and Brehm, M.A. (2016). Improved B cell development in humanized NOD-scid IL2Rγnull mice transgenically expressing human stem cell factor, granulocyte-macrophage colony-stimulating factor and interleukin-3. Immun. Inflamm. Dis. *4*, 427–440.
75. Ishikawa, F., Yasukawa, M., Lyons, B., Yoshida, S., Miyamoto, T., Yoshimoto, G., Watanabe, T., Akashi, K., Shultz, L.D., and Harada, M. (2005). Development of functional human blood and immune systems in NOD/SCID/IL2 receptor {gamma} chain(null) mice. Blood *106*, 1565–1573.
76. Lepus, C.M., Gibson, T.F., Gerber, S.A., Kawikova, I., Szczepanik, M., Hossain, J., Ablamunits, V., Kirkiles-Smith, N., Herold, K.C., Donis, R.O., et al. (2009). Comparison of human fetal liver, umbilical cord blood, and adult blood hematopoietic stem cell engraftment in NOD-scid/gammac-/-Balb/c-Rag1-/-gammac-/-, and C.B-17-scid/bg immunodeficient mice. Hum. Immunol. *70*, 790–802.
77. Matsumura, T., Kametani, Y., Ando, K., Hirano, Y., Katano, I., Ito, R., Shiina, M., Tsukamoto, H., Saito, Y., Tokuda, Y., et al. (2003). Functional CD5+ B cells develop predominantly in the spleen of NOD/SCID/gammac(null) (NOG) mice transplanted either with human umbilical cord blood, bone marrow, or mobilized peripheral blood CD34+ cells. Exp. Hematol. *31*, 789–797.
78. Katano, I., Ito, R., Kamisako, T., Eto, T., Ogura, T., Kawai, K., Suemizu, H., Takahashi, T., Kawakami, Y., and Ito, M. (2014). NOD-Rag2null IL-2Rγnull mice: an alternative to NOG mice for generation of humanized mice. Exp. Anim. *63*, 321–330.
79. Traggiai, E., Chicha, L., Mazzucchelli, L., Bronz, L., Piffaretti, J.C., Lanzavecchia, A., and Manz, M.G. (2004). Development of a human adaptive immune system in cord blood cell-transplanted mice. Science *304*, 104–107.
80. Comprehensive Evaluation of Human Immune System Reconstitution in NSG and NSG-SGM3 Mouse Models. https://resources.jax.org/white-papers/whitepaper-onco-hu-2.
81. Lepone, L.M., Donahue, R.N., Grenga, I., Metenou, S., Richards, J., Heery, C.R., Madan, R.A., Gulley, J.L., and Schlom, J. (2016). Analyses of 123 Peripheral Human Immune Cell Subsets: Defining Differences with Age and between Healthy Donors and Cancer Patients Not Detected in Analysis of Standard Immune Cell Types. J. Circ. Biomark. *5*, 5.
82. Brodaczewska, K.K., Szczylik, C., Fiedorowicz, M., Porta, C., and Czarnecka, A.M. (2016). Choosing the right cell line for renal cell cancer research. Mol. Cancer *15*, 83.
83. Zhang, Z., Liu, J., Zhang, C., Li, F., Li, L., Wang, D., Chand, D., Guan, F., Zang, X., and Zhang, Y. (2020). Over-Expression and Prognostic Significance of HHLA2, a New Immune Checkpoint Molecule, in Human Clear Cell Renal Cell Carcinoma. Front. Cell Dev. Biol. *8*, 280.
84. Bhatt, R.S., Berjis, A., Konge, J.C., Mahoney, K.M., Klee, A.N., Freeman, S.S., Chen, C.H., Jegede, O.A., Catalano, P.J., Pignon, J.C., et al. (2021). KIR3DL3 Is an Inhibitory Receptor for HHLA2 that Mediates an Alternative Immunoinhibitory Pathway to PD1. Cancer Immunol. Res. *9*, 156–169.
85. Sobczuk, P., Brodziak, A., Khan, M.I., Chhabra, S., Fiedorowicz, M., Wełniak-Kamińska, M., Synoradzki, K., Bartnik, E., Cudnoch-Jędrzejewska, A., and Czarnecka, A.M. (2020). Choosing The Right Animal Model for Renal Cancer Research. Transl. Oncol. *13*, 100745.
86. Shultz, L.D., Saito, Y., Najima, Y., Tanaka, S., Ochi, T., Tomizawa, M., Doi, T., Sone, A., Suzuki, N., Fujiwara, H., et al. (2010). Generation of functional human T-cell subsets with HLA-restricted immune responses in HLA class I expressing NOD/SCID/IL2r gamma(null) humanized mice. Proc. Natl. Acad. Sci. USA *107*, 13022–13027.
87. Stadtmauer, E.A., Fraietta, J.A., Davis, M.M., Cohen, A.D., Weber, K.L., Lancaster, E.,

Mangan, P.A., Kulikovskaya, I., Gupta, M., Chen, F., et al. (2020). CRISPR-engineered T cells in patients with refractory cancer. Science *367*, eaba7365.

88. Rupp, L.J., Schumann, K., Roybal, K.T., Gate, R.E., Ye, C.J., Lim, W.A., and Marson, A. (2017). CRISPR/Cas9-mediated PD-1 disruption enhances anti-tumor efficacy of human chimeric antigen receptor T cells. Sci. Rep. *7*, 737.
89. Strauss, L., Mahmoud, M.A.A., Weaver, J.D., Tijaro-Ovalle, N.M., Christofides, A., Wang, Q., Pal, R., Yuan, M., Asara, J., Patsoukis, N., and Boussiotis, V.A. (2020). Targeted deletion of PD-1 in myeloid cells induces antitumor immunity. Sci. Immunol. *5*, eaay1863.
90. Odorizzi, P.M., Pauken, K.E., Paley, M.A., Sharpe, A., and Wherry, E.J. (2015). Genetic absence of PD-1 promotes accumulation of terminally differentiated exhausted CD8+ T cells. J. Exp. Med. *212*, 1125–1137.
91. Riley, R.S., June, C.H., Langer, R., and Mitchell, M.J. (2019). Delivery technologies for cancer immunotherapy. Nat. Rev. Drug Discov. *18*, 175–196.
92. Rafiq, S., Yeku, O.O., Jackson, H.J., Purdon, T.J., van Leeuwen, D.G., Drakes, D.J., Song, M., Miele, M.M., Li, Z., Wang, P., et al. (2018). Targeted delivery of a PD-1-blocking scFv by CAR-T cells enhances anti-tumor efficacy in vivo. Nat. Biotechnol. *36*, 847–856.
93. Monaco, G., Lee, B., Xu, W., Mustafah, S., Hwang, Y.Y., Carré, C., Burdin, N., Visan, L., Ceccarelli, M., Poidinger, M., et al. (2019). RNA-Seq Signatures Normalized by mRNA Abundance Allow Absolute Deconvolution of Human Immune Cell Types. Cell Rep. *26*, 1627–1640.e7.
94. Grieshaber-Bouyer, R., Radtke, F.A., Cunin, P., Stifano, G., Levescot, A., Vijaykumar, B., Nelson-Maney, N., Blaustein, R.B., Monach, P.A., and Nigrovic, P.A.; ImmGen Consortium (2021). The neutrotime transcriptional signature defines a single continuum of neutrophils across biological compartments. Nat. Commun. *12*, 2856.
95. Lan, P., Wang, L., Diouf, B., Eguchi, H., Su, H., Bronson, R., Sachs, D.H., Sykes, M., and Yang, Y.G. (2004). Induction of human T-cell tolerance to porcine xenoantigens through mixed hematopoietic chimerism. Blood *103*, 3964–3969.
96. Melkus, M.W., Estes, J.D., Padgett-Thomas, A., Gatlin, J., Denton, P.W., Othieno, F.A., Wege, A.K., Haase, A.T., and Garcia, J.V. (2006). Humanized mice mount specific adaptive and innate immune responses to EBV and TSST-1. Nat. Med. *12*, 1316–1322.
97. Magiera-Mularz, K., Kocik, J., Musielak, B., Plewka, J., Sala, D., Machula, M., Grudnik, P., Hajduk, M., Czepiel, M., Siedlar, M., et al. (2021). Human and mouse PD-L1: similar molecular structure, but different druggability profiles. iScience *24*, 101960.
98. Costa, M.J., Kudaravalli, J., Liu, W.H., Stock, J., Kong, S., and Liu, S.H. (2018). A mouse model for evaluation of efficacy and concomitant toxicity of anti-human CXCR4 therapeutics. PLoS One *13*, e0194688.
99. Hao, Y., Hao, S., Andersen-Nissen, E., Mauck, W.M., 3rd, Zheng, S., Butler, A., Lee, M.J., Wilk, A.J., Darby, C., Zager, M., et al. (2021). Integrated analysis of multimodal single-cell data. Cell *184*, 3573–3587.e29.
100. Korsunsky, I., Millard, N., Fan, J., Slowikowski, K., Zhang, F., Wei, K., Baglaenko, Y., Brenner, M., Loh, P.R., and Raychaudhuri, S. (2019). Fast, sensitive and accurate integration of single-cell data with Harmony. Nat. Methods *16*, 1289–1296.
101. Testi, M., and Andreani, M. (2015). Luminex-Based Methods in High-Resolution HLA Typing. Methods Mol. Biol. *1310*, 231–245.
102. Stoeckius, M., Zheng, S., Houck-Loomis, B., Hao, S., Yeung, B.Z., Mauck, W.M., Smibert, P., and Satija, R. (2018). Cell Hashing with barcoded antibodies enables multiplexing and doublet detection for single cell genomics. Genome Biol. *19*, 224.
103. Germain, P.L., Lun, A., Garcia Meixide, C., Macnair, W., and Robinson, M.D. (2021). Doublet identification in single-cell sequencing data using scDblFinder. F1000Res. *10*, 1–23.

STAR★METHODS

KEY RESOURCES TABLE

REAGENT or RESOURCE	SOURCE	IDENTIFIER
Antibodies		
Goat-anti human IgG-Fc	Bethyl Laboratories	A80-104A
MSD SULFO-TAG Labeled Anti-Human Antibody (Goat)	MSD	R32AJ-1
Anti-human CD45 PerCP/Cy5.5	BioLegend	304028
Anti-mouse CD45 Dazzle594	BioLegend	103146
Anti-human CD3 BV650	BioLegend	317324
Anti-human CD4 AF700	BioLegend	357418
Anti-human CD8 BV785	BioLegend	344740
Anti-human CD19 BV421	BioLegend	302234
Anti-human CD27 BV711	BioLegend	356430
Anti-human CD62L BV510	BioLegend	304844
Anti-human PD1 PE	BD	557946
Anti-human TIM-3 APC/Cyanine7	BioLegend	345026
Anti-human CD45RA PerCP/Cyanine5.5	BioLegend	304122
Anti-human CD45RO PE/Cyanine7	BioLegend	304230
Bacterial and virus strains		
pHAGE-Ef1a-IRES-WPRE	This paper	N/A
Biological samples		
Leukopak	StemCell	70500
Apheresis leukoreduction collars	obtained from the blood bank of the Brigham and Women's Hospital under DFCI approved IRB protocol #14-343	N/A
Chemicals, peptides, and recombinant proteins		
Polyethylenimine, PEI		
Lenti-X™ Concentrator	Clontech	631231
Ficoll-Paque-PLUS	GE Healthcare	45001750
Gentamicin	Gibco	15750060
IL-21	Miltenyi Biotec	130-095-784
IL-7	Miltenyi Biotec	130-095-363
IL-15	Miltenyi Biotec	130-095-765
D-luciferin potassium salt	Promega	E1605
Critical commercial assays		
Zombie Yellow™ Fixable Viability Kit	BioLegend	423104
Tumor Dissociation Kit	Miltenyi Biotec	130-095-929
CD34 microbead kit	Miltenyi Biotec	130-100-453
CD4 microbeads	Miltenyi Biotec	130-097-048
CD8 microbeads	Miltenyi Biotec	130-097-057
TransAct kit	Miltenyi Biotec	130-111-160
Deposited data		
scRNAseq data	This paper	GSE210664

(*Continued on next page*)

Continued

REAGENT or RESOURCE	SOURCE	IDENTIFIER
Kevin Bi et al.	Single Cell Portal	Single Cell Portal: https://singlecell.broadinstitute.org/single_cell/study/SCP1288/tumor-and-immune-reprogramming-during-immunotherapy-in-advanced-renal-cell-carcinoma#study-summary
Codes	This paper	https://doi.org/10.5281/zenodo.7274663
Supplementary tables	This paper; Zenodo Data	Table S2~10; https://doi.org/10.5281/zenodo.10456704
Software and algorithms		
Cellranger	10x genomics	https://www.10xgenomics.com/support/software/cell-ranger
Seurat	Hao et al.[99]	https://satijalab.org/seurat/
harmony	Korsunsky et al.[100]	https://portals.broadinstitute.org/harmony/index.html
CellChat	Jin et al.[64]	https://github.com/sqjin/CellChat
Velocyto	La Manno et al.[50]	https://velocyto.org/

RESOURCE AVAILABILITY

Lead contact

Further information and requests for resources and reagents should be directed to and will be fulfilled by the lead contact, Wayne Marasco (wayne_marasco@dfci.harvard.edu).

Materials availability

All plasmids and cell lines used in this paper will be shared by the lead contact upon request.

Data and code availability

All generated scRNAseq data are available at the Gene Expression Omnibus (GEO) with accession code GSE210664. Supplementary Tables from 2 to 10 can be found in https://doi.org/10.5281/zenodo.10456704. Original codes can be accessed via https://doi.org/10.5281/zenodo.7274663. Any additional information required to reanalyze the data reported in this paper is available from the lead contact upon request.

EXPERIMENTAL MODEL AND STUDY PARTICIPANT DETAILS

Cell lines and culture

Human clear cell renal cell carcinoma cell line skrc-59 (obtained from Dr. Gerd Ritter, Memorial Sloan Kettering Cancer Center, New York, USA) was engineered to express high levels of human CAIX (skrc-59 CAIX+)[30] and mCardinal fluorescent protein. These cells were grown in RPMI-1640 medium (Gibco) supplemented with 10% (v/v) heat-inactivated fetal bovine serum (FBS, Gibco) at 37°C with 5% CO_2.

Ethical approval

Apheresis leukoreduction collars were obtained from the blood bank of the Brigham and Women's Hospital under DFCI approved IRB protocol #14–343. Humanized mouse model experiments were performed under DFCI approved protocol #05–035.

METHODS DETAILS

Production of lentivirus particles

For lentivirus production, polyethylenimine (PEI), DNA of the helper plasmids VSVG, TAT, GAG and REV (10 μg per 15 cm dish of 293T cells) and 20 μg of the respective CAR DNA were added to Opti-MEM medium (Gibco). This mixture was incubated for 20 min at RT and was afterward added drop by drop to a 15 cm dish of LentiX-293T cells (Clontech). After 48 h of incubation, the supernatant was collected, debris was removed and lentiviral concentrator (Clontech) was added in a 1:3 (v/v) ratio. This mixture was incubated overnight at 4°C, the next day the tubes were centrifuged for 45 min at 1,500 g and the supernatant was discarded. The pelleted lentivirus was resuspended in RPMI-1640 medium and stored at −80°C.

Generation of CAR-T cells

A leukopak (StemCell) and apheresis leukoreduction collars (blood bank of the Brigham and Women's Hospital) were obtained under DFCI approved IRB protocol #14–343. Human peripheral blood mononuclear cells (PBMCs) were separated using Ficoll-Paque-PLUS (GE Healthcare). CD4 and CD8 T cells were isolated by positive selection using CD8 MicroBeads and CD4 MicroBeads (Miltenyi Biotec) respectively. T cells were cultured in RPMI-1640 medium supplemented with 10% FBS, IL-21 (30 ng/mL, Miltenyi Biotec) and activated by T cell TransAct (Miltenyi Biotec). CAR-T cells were generated by lentiviral transduction (MOI 20) with 10 μg/mL Diethylaminoethyl (DEAE). The CAR positive T cells were sorted by SONY sorter MA900. After sorting, the T cells were cultured in RPMI-1640 medium supplemented with 10% FBS, IL-7 (5 ng/mL, Miltenyi Biotec), IL-15 (2.5 ng/mL, Miltenyi Biotec) and Gentamicin (50 μg/mL) (Gibco).

Payload quantification

Standard MSD High Bind Plates were coated with 25 μL of goat-anti human IgG-Fc fragment (affinity purified: A80-104A) diluted to 1 μg/mL in PBS. After centrifugation at 500xg for 1 min, plates were incubated overnight at 4C. The following day, plates were washed with 50 μL PBS per well blocked with 25 μL 1% BSA in PBS per well, centrifuged at 500xg for 1 min, and incubated overnight at 4C. The following day, plates were washed 3 times with 50 μL PBS per well before adding 25 μL of samples diluted 4-fold in 1% BSA in PBS. Samples were centrifuged at 500xg for 1 min, and incubated on a shaker for 2 h at room temperature. Plates were then washed 3 times with 50 μL PBS per well before adding 25 μL of detection antibody (MSD SULFO-TAG Labeled Anti-Human Antibody (Goat), catalog #R32AJ-1) at 1 μL/mL diluted in PBS per well, followed by incubation for 1 h at room temperature, and 5 washes with 50 μL PBS. 35 μL per well 1X MSD read buffer with surfactant diluted in water was added and the plates were read using MESO SECTOR S 600.

HLA typing

HLA typing was performed by American Red Cross HLA Laboratory (Dedham, MA) using molecular SSO (Luminex).[101]

In vitro killing assay

Celigo *in vitro* killing assay was performed as described before.[31,38] Approximately 3000 skrc-59 tumor cells (target cells) were seeded in a 96-well plate (Greiner 655090). After 12 h of incubation, the plate was scanned and analyzed in bright field and far red channel for mCardinal as the 0 h time point. CAR-T cells were added and co-incubated with the target cells. Additional control wells were prepared with target cells only (negative control) and target cells with 1% Triton X-(positive control). Subsequently, the plate was scanned and analyzed at the 48 h time point with the equation, $Cytotoxicity\ \% = \frac{negative\ control - treatment}{negative\ control - positive\ control} \times 100$.

Flow cytometry

All samples were analyzed with an LSR Fortessa (BD Bioscience) and data were analyzed using FlowJo software (FlowJo LLC). T cell phenotype was evaluated via:Zombie Yellow Fixable Viability Kit (BioLegend), human CD45 (clone HI30, BioLegend), mouse CD45 (clone 30F11, BioLegend), CD3 (clone OKT3, BioLegend), CD4 (clone A161A1, BioLegend), CD8 (clone SK1, BioLegend), CD19 (clone HIB19, BioLegend), CD27 (clone M-T271, BioLegend), CD62L (DREG-56, BioLegend), PD-1 (clone MIH4, BD Bioscience), TIM-3 (clone F38-2E2, BioLegend), CD45RO (clone UCHL1, BioLegend), CD45RA (HI100, BioLegend).

In vivo orthotopic humanized ccRCC model

Humanized mouse model was established based on publication reported before[25] and performed under DFCI approved protocol #05–035. CD34 HSCs were isolated from an 18-week-old fetal liver tissue using CD34 microbeads (Miltenyi Biotec), which was 4/6 HLA matched to the skrc-59 tumor cell line. One hundred thousand $CD34^+$ HSCs were injected intrahepatically in 1–4 days old neonates irradiated with a single sublethal dose of 1 Gy whole body irradiation. After 12 weeks, humanized mice were bled to assess the humanization efficiency. Once the humanization was matured (human CD45 > 20% is considered successfully humanized), 50,000 skrc-59 $CAIX^+$ $luciferase^+$ cells were resuspended in 10 μL of RPMI-1640 medium and diluted 1: 1 in Matrigel (Corning). This cell mixture was injected under the left kidney capsule of NSG-SGM3 mice (Jackson Laboratories). One week after, tumor engraftment was confirmed with bioluminescence (BLI) imaging and 1 million CAR-T cells or untransduced T cells were injected through the tail vein of the mice (Day 0, N = 5 mice per group). The tumor BLI was determined 14 days post CAR-T cell injection. On Day 28, the mice were sacrificed by CO_2 inhalation, final blood was drawn and organs and tumors were harvested for analysis.

Bioluminescence imaging (BLI)

Tumor growth was monitored at Day 0 and 14 using the IVIS Spectrum *In Vivo* Imaging System (PerkinElmer). Briefly, mice were injected subcutaneously with 75 mg/kg D-luciferin potassium salt (Promega E1605) in sterile PBS and anesthetized with 2% isoflurane in medical air. Serial bioluminescence images were acquired using the automated exposure set-up. The peak bioluminescence signal intensity within selected regions of interest (ROIs) was quantified using the Living Image Software (PerkinElmer), and expressed as photon flux (p/sec/cm2/sr). Representative planar bioluminescence images were displayed with indicated adjusted minimal and maximal thresholds.

Tumor dissociation and tumor infiltrating CAR-T cell isolation

Renal tumor samples were dissociated into single cells by a semi-automated combined mechanical/enzymatic process. The tumor tissue was cut into pieces of (2-3mm) in size and transferred to C Tubes (Miltenyi Biotech) containing a mix of Enzymes H, R and A (Tumor Dissociation Kit, human; Miltenyi Biotech). Mechanical dissociation was accomplished by performing a program (37C_h_TDK_1) on the gentleMAC Octo Dissociator with Heaters (Miltenyi Biotech). Single cell suspensions generated from ccRCC tumor samples were FACS sorted on a SONY MA900 sorter (SONY) for viable human TILs (Zombie-mCD45-hCD45+, BioLegend).

RNA-seq 10X genomics library preparation, hash tag, and single cell 5′ sequencing

Single-cell RNA-seq experiments were performed by the Brigham and Women's Hospital Center for Cellular Profiling. Sorted cells were stained with a distinct barcoded antibody (Cell-Hashing antibody, TotalSeq-C, Biolegend) as previously described.[102] After washing, the stained cells were resuspended in 0.4% BSA in PBS at a concentration of 2,000 cells per μL, then loaded onto a single lane (Chromium chip K, 10X Genomics) followed by encapsulation in a lipid droplet (Single Cell 5′kit V2, 10X Genomics) followed by cDNA and library generation according to the manufacturer's protocol. 5′ mRNA library was sequenced to an average of 50,000 reads per cell, V(D)J library and protein (hashtags) library sequenced to an average of 15,000 reads per cell, all using Illumina Novaseq.

Data processing

Since our sample contained an artificial gene construct (CAR sequence), we added the 5-prime part of the CAR sequences by using mkref function in the Cell Ranger software (v6.1.2) (Table S1). Using the modified genome, we obtained a gene-count matrix with a hashtag for each group from the first experiment (group 1, 2, 3, 4, 5) from raw fastq files of scRNAseq and CITEseq data. We also used Cell Ranger (v4.0.0) to obtain a clonotype for each cell from raw fastq files of VDJ-seq data with only the productive TCR sequence. First, we filtered out a potential doublet by scDblfinder[103] (v1.2.0) with default parameters. Second, we used the Seurat package[99] (v 4.0.6) for preprocessing and downstream analysis of the data. We filtered cells by discarding the cells that had high contamination of mitochondrial genes or those which were outliers in nfeatures_RNA and nCount_RNA from the "FeatureScatter" plot. Third, we distinguished each group by HTODemux function with default parameters. We only retained the unique hashtag for each group. Finally, we merged scRNAseq data with VDJ-seq data by saving only the cells that had paired data for scRNAseq and VDJ-seq in T cells. We performed the same procedure for the second experiment except de-multiplexing since scRNAseq for groups 1, 2, and 3 was conducted separately.

Merging and batch correction of main celltypes

After merging the Seurat objects together, we applied "NormalizeData" as the recommended setting for each patient (Log-normalization, scale factor:10,000). We used 2,000 highly variable genes for downstream analysis, such as dimension reduction and clustering. "ScaleData," "RunPCA," and "RunUMAP" functions were used with default settings. We ran Harmony[100] (version 0.1.0) with 1∼50 PCs to correct the batch effect between each sample from each main cell type, respectively. After batch correction, "RunUMAP" functions in Seurat v4 were utilized for dimension reduction and visualization using default settings, except for giving the reduction parameter as "harmony". Unsupervised clustering was performed by "FindNeighbors," which conducts shared-nearest-neighbor-based clustering with highly variable genes, and "FindClusters" which conducts Louvain clustering with the resolution 0.3. During the procedure, we further removed cancer cells or bad cells. Finally, T cells, B cells, and Myeloid cells were identified by their marker genes (Table S2) from differentially expressed gene (DEG) by "FindAllMarkers". DEGs were defined by |avgLog2FC| > 0.25, min.pct <0.25, and adjusted p value <0.01 (Table S3).

Subclustering of myeloid and T cells

We further subclustered the myeloid and T cells with another round of processing as above. For myeloids, we used 1–30 PCs for the analysis with 0.4 resolution for the clustering parameter. We found 5 subclusters from myeloid cells and annotated with a marker gene list (Table S2) from DEG as above (Table S8).

For T cells, after excluding TCR genes from the variable gene list, we used Seurat integration method (PC: 1–40) to merge the T cells from different samples for subclustering, we split the data into CD4 T cells, CD8 T cells, NK lineage, and cycling T cells based on the distribution of CD4, CD8A, cycling markers (MKI67 and TOP2A), NK markers (TYROBP and NCAM1), and T cell markers (CD3D, CD3E, CD3G). For each compartment, we conducted another round of clustering for fine clustering. Annotation of cell type was defined by DEG using all the T cells, CD4 T cells only, and CD8 T cells only (Tables S2 and S5).

Data transferring to human ccRCC data

We downloaded processed scRNAseq data[18] from Single Cell Portal (https://singlecell.broadinstitute.org/single_cell/study/SCP1288/tumor-and-immune-reprogramming-during-immunotherapy-in-advanced-renal-cell-carcinoma#study-summary). We obtained clinical information and meta data from the supplementary material. We followed the original cell type annotation for our analysis. We performed data-transferring by Seurat package with "FindTransferAnchors" and "MapQuery" functions.

T cell clonality analysis

We obtained clonal type of T cells from the "clonotypes.csv" output of cellranger pipeline. We assigned a cell as "multiplet" if a given T cell shared the same clonotype with other T cells in each sample. Otherwise, we assigned it as "singlet". If the TCR sequence was not available for a given T cell, we did not consider it for the clonotype analysis.

Cell abundance analysis

The relative abundance of each cell type was measured by normalizing the total number of cell counts in each group. We performed a Fisher's exact test between the two different groups to obtain a p value. Benjamini-Hochberg correction was conducted to obtain adjusted p values. We considered adjusted $|FC| > 2$ and p value <0.01 as a significant difference (Table S4).

Signature analysis

We measured the signature score by "AddModuleScore" function in Seurat package. The list of genes for each Table S7. We used the same size of a given genes for "ctrl" parameter. We used the average score from the results of "AddModuleScore" for each cell. While comparing between two groups, we performed Wilcoxon rank-sum test to obtain p values.

DEG analysis between groups

The DEG analysis to compare between two groups was conducted by using "FindMarkers" function in Seurat package. DEGs were defined by $|avgLog2FC| > 0.25$, min.pct <0.25, and adjusted p value <0.01 (Table S10).

Cell-cell interaction analysis

We used CellChat[64] (v1.4.0) to infer the interaction between celltypes. We followed the tutorial pipeline. In detail, we used the receptor-ligand database provided by cellchat. "subsetData", "identifyOverExpressedGenes", "identigyOverExpressedInteractions", "computeCommunProb", "filterCommunication", and "computeCommunProbPathway" functions were used (Table S9).

RNA velocity analysis

We used velocyto[50] (v0.17.16) to infer the RNA velocity with default pipeline. But we used previous results of variable genes, UMAP coordinate from Seurat package. We obtained the transition probability from the "transition_prob.T" variable (Table S6).

QUANTIFICATION AND STATISTICAL ANALYSIS

The data are presented as mean $\pm$ s.d. as indicated in the figure legends. For comparisons between groups, the data were analyzed by one-way ANOVA analysis. All statistical analyses were performed using GraphPad Prism software. The calculated p values are reported using the symbols: 'n.s.' means not significant, '*' means $p < 0.05$, '**' represents $p < 0.01$, and '***' stands for $p < 0.001$.